CHAPTER SIX

The role of membrane vesiculation and encapsulation in cancer diagnosis and therapy

Mitja Drab[a,b,*], Luka Mesarec[a], Roghayeh Imani[c], Marko Jeran[a,d], Ita Junkar[e], Veronika Kralj-Iglič[d,h], Samo Kralj[f,g] and Aleš Iglič[a,b,h]

[a]Laboratory of Physics, Faculty of Electrical Engineering, University of Ljubljana, Ljubljana, Slovenia
[b]Laboratory of Clinical Biophysics, Chair of Orthopaedic Surgery, Faculty of Medicine, University of Ljubljana, Ljubljana, Slovenia
[c]Department of Engineering Sciences and Mathematics, Luleå University of Technology, Luleå, Sweden
[d]Laboratory of Clinical Biophysics, Faculty of Health Sciences, University of Ljubljana, Ljubljana, Slovenia
[e]Department of Surface Engineering and Optoelectronics, "Jožef Stefan" Institute, Ljubljana, Slovenia
[f]Condensed Matter Physics Department, "Jožef Stefan" Institute, Ljubljana, Slovenia
[g]Faculty of Natural Sciences and Mathematics, University of Maribor, Maribor, Slovenia
[h]Institute of Biosciences and BioResources, National Research Council of Italy, Italy
*Corresponding author: E-mail: mitja.drab@fe.uni-lj.si

Contents

Abstract

We summarize recent findings and advances in cancer diagnostics in relation to extracellular vesicles (EVs) and emerging therapeutic options of nanomaterials. We revise the common mechanism for EV inception, vesiculation, through a physical model of the liquid mosaic membrane with laterally mobile membrane rafts that determine local spontaneous curvature. If such in-plane orientational ordering is present, we show that spatial non-homogeneities may trigger energetically favourable membrane

Advances in Biomembranes and Lipid Self-Assembly, Volume 29
ISSN 2451-9634
https://doi.org/10.1016/bs.abl.2019.01.007

vesiculation. In addition, we revise a novel technique of cancer therapy using multifunctional titanium nanobeads (NBs) that form a fully biocompatible system used for optical imaging, magnetic resonance imaging and selective reactive oxygen species photogeneration. We study the encapsulation of these functional NBs theoretically with Monte Carlo (MC) simulations and find that the wrapping transition depends on the strength of mobile charges, giving insight into future functional optimization for maximum therapeutic benefit.

1. Introduction

The number of people living with a cancer diagnosis worldwide reached nearly 14.5 million in 2014 and is expected to rise to almost 19 million in 2024, urging the development of new diagnostic methods of suppressing, or even selectively killing, cancer cells in the human body [1–4]. With more than 100 distinct types of human cancer having been described, while subtypes of tumors can be found within specific organs, it is understood that cancer is a highly complex disease both in a spatial and temporal dimension [5]. With recent developments in the nanosciences, particularly in engineering and medicine at the scales of micro- or nanometers, extensive work has been devoted to chemical and biological methods involving specific molecules, pathways, reactions and particle binding. Although substantial progress has been made in particular cases, there is still no consensus on essential underlying mechanisms of tumor inception, growth and proliferation. However, cancer progression is almost always correlated to changes in cellular morphology, which hints at the fact that the role of physics, underlying these changes, should not be understated. There is evidence to believe that function precedes, even dictates, shape in many biological processes, both at the level of cells and molecules. An example of the former is the typical invagination of the embryo during gastrulation of the fruit fly, which takes place after the first cell differentiation [6]. At a molecular level, the functions of many proteins rely on their three dimensional shapes. For example, hemoglobin forms a cavity into which the protein heme, which binds to oxygen, comfortably sits [7]. Here morphological changes couple to electrostatic interactions and changes of the thermodynamic free energy, which are physical quantities. Although living systems are far too complex to be understood purely in physical terms, there is insight to be hand studying them theoretically through simplified models.

In this review, we present two recent key advances in cancer diagnostics and therapeutics and discuss respective physical models that sufficiently

explain these phenomena on the scale of biological membranes. First, we look at evidence that cancer proliferation is substantially aided by the creation of extracellular vesicles (EVs) that pinch off the parent cell and are able to circulate freely to other parts of the organism. In regards to cell membrane composition, we present a possible mechanism of membrane fission (vesiculation) with in-plane ordering and topological defects that could underlie such processes.

Next, we discuss a recently reported nanoparticle therapy which integrates therapeutics with diagnostics — also known as theranostics — using multifunctional mesoporous gadolinium-doped TiO_2 nanobeads (Gd@titania NBs) possessing a high degree of stability and biocompatibility. We will see that Gd@titania NBs form a fully biocompatible system for optical imaging (OI), magnetic resonance imaging (MRI) and selective ROS (anticancer agent) photo-generation inside the cancer cells, providing impressive multi-functionality and allowing for simultaneous OI-MRI and photodynamic therapy (PDT) without compromising the advantages of either component [8]. The endocytosis of these in cancerous cells NBs is evaluated with the aid of numerical (Monte Carlo) and experimental results, demonstrating that cellular internalization is directly linked to physical properties of cell membranes [9].

2. Extracellular vesicles as diagnostic biomarkers for cancer

The growth and proliferation of cancer within the body is strongly dependent on a variety of mechanisms that take place at the cellular scales and below [4]. EVs are little buds pinched from the cell and ubiquitous in most bodily fluids [10,11] including malignant ascites [12], blood plasma [13], saliva [14] and urine [15], reflecting the composition of the parent cell, while also conveying matter and information between cells and taking part in spreading of inflammation, infection and tumors [3,16]. EVs influence various physiological and pathological functions of both recipient and parent cells, having been found to transfer surface-bound ligands and receptors [17], prion proteins [18], genetic material including RNA [19], and infectious particles between healthy and cancerous cells alike [10,20,21]. Their presence in biological fluids offers unprecedented, remote, and non-invasive access to crucial molecular information about the health status of cells, including their driver mutations, classifiers, molecular subtypes, therapeutic targets, and biomarkers of drug resistance. However,

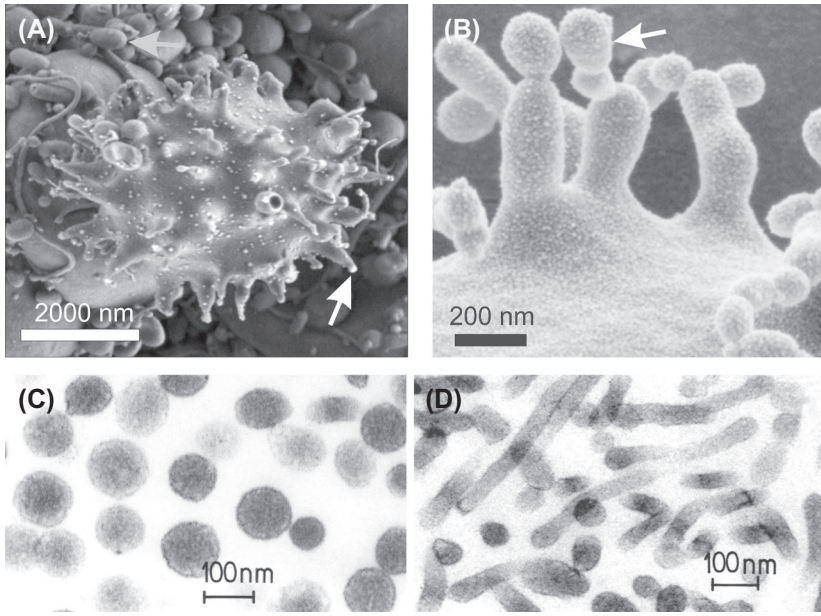

Figure 1 Budding of an erythrocyte membrane (A, B) and isolated extracellular vesicles (C, D). Buds are formed on the tips of the echinocyte spiculae found in the isolate from blood (A, white arrow). Numerous globule-shaped extracellular vesicles are present in the isolates (A, gray arrow). Extracellular vesicles shown in panels (C) and (D) were isolated from red blood cell suspension treated with detergent: dodecyl-zwittergent (C) and dodecyl-maltoside (D). Panels (A) and (B) show scanning electron micrographs and panels (C) and (D) show transmission electron micrographs. *Adapted from V. Kralj-Iglič, A. Iglič, H. Hägerstrand, M. Bobrowska-Hägerstrand, Hypothesis of nanostructures of cell and phospholipid membranes as cell infrastructure. Med. Razgl. 44 (2005) 155–169; V. Šuštar, A. Bedina-Zavec, R. Štukelj, M. Frank, G. Bobojević, R. Janša, E. Ogorevc, P. Kruljc, K. Mam, B. Šimunič, Nanoparticles isolated from blood: a reflection of vesiculability of blood cells during the isolation process, Int. J. Nanomed. 6 (2011) 2737; V. Suštar, A. Bedina-Zavec, R. Stukelj, M. Frank, E. Ogorevc, R. Janša, K. Mam, P. Veranič, and V. Kralj-Iglič, Post-prandial rise of microvesicles in peripheral blood of healthy human donors, Lipids Health Dis. 10 (2011) 47–47.*

much work is still needed to elucidate the specific details of EV properties, standardize isolation techniques and diagnostic protocols (Fig. 1).

EVs are created in the membrane budding process in a variety of cell types however, more frequently, in tumor cells. The analysis of EVs isolated from selected tumor types is presented in Table 1. It has been found that EVs contain various cancer markers such as tumor suppressors, phosphoproteins, surface antigens and proteases [25], oncogenic epidermal growth factor receptor, microRNAs [26] etc. and that the function of the original cell

Table 1 Extracellular vesicle expression in various types of tumors.

Tumor type	Comments	References
Ovarian	Malignant vesicles stimulated invasion; the combination of ovarian cancer cells and membrane vesicles resulted in greater uPA activation; vesicles from malignant ascites were also found to contain activated MMP-2, MMP-9, and uPA.	[30]
Ovarian	Higher levels of miRNAs correlated with advanced ovarian cancer.	[31]
Breast	MicroRNA-200 family is enriched in the serum of patients with metastatic cancers.	[32]
Breast	The expression of transient receptor potential channel 5 (TrpC5) proteins was high in the tumor.	[33]
Prostate	The concentration of EVs was higher in the cancer patients than in the healthy controls; EVs derived from prostate cancer cell lines carry different gDNA content.	[34]
Colorectal	SW620 EVs-enriched proteins overexpressed in metastatic colorectal cancer cells.	[35]
Hepatocellular	Long non-coding RNA enriched within extracellular vesicles derived from tumor cells.	[36]
Bladder	Different expression of epithelial–mesenchymal transition (EMT) factors in metastatic and nonmetastatic human bladder carcinoma cells.	[37]
Pancreatic	Glypican-1 (GPC1) enriched on cancer-cell-derived exosomes.	[38]
Lung	Microvesicles derived from activated platelets induce metastasis and angiogenesis in lung cancer.	[39]

can be extrapolated by examining EV composition. EVs offer a dual potential as diagnostic tools as well as therapeutic agents for cancer treatment. They can be utilized for early detection of diseases, the monitoring of therapeutic responses, and the targeted delivery of therapeutic agents, offering a non-invasive means to assess cancer initiation, progression and treatment outcomes [1].

An example of recent research demonstrates that tumors of various origin and various clinical outcomes can be classified by their micro RNA (miRNA) profiles, of which over 700 have been identified in the human genome [27]. miRNA profiling has already been used to determine whether

patients with chronic lymphocytic leukemia have slow-growing or aggressive forms of cancer [28], while plasma samples collected from patients with early (stage II) colorectal cancer could be distinguished from those of healthy gender-matched and age-matched volunteers [29]. Differentiation of various EVs found in body fluids could potentially lead to an alternative forms of disease identifying, as blood assessment is much less invasive than current methods of diagnosing malignancies.

It is possible to consider vesiculation of EVs as a process that is determined by lipid membrane transformation induced through curvature and membrane constituents. Considering the symmetry of membrane constituents, it is found that cell shape and budding follows energetically favorable configurations in regions where strong curvature anisotropy is present. Remarkably, these theoretical predictions are supported by experimental evidence, both in living cells [40] or artificially produced exosomes [41].

2.1 The fluid mosaic model of the membrane

In 1972, Singer and Nicolson proposed a fluid mosaic model of the membrane, viewing it generally as a lipid bilayer with embedded proteins and large molecules [42]. Physically, such a model considers the phospholipid bilayer as a two-dimensional laterally isotropic liquid, with proteins and other larger molecules free to move within it. Many experiments in the last decades have established the fluid mosaic model as the standard description of the cell membrane. In the late 1990s, this model was advanced including also lateral inhomogeneities in the membrane matrix. In the two-dimensional liquid membrane phase micro-domains of specific composition called membrane rafts were envisioned, which are small (10–200 nm), dynamic structures with an increased concentration of cholesterol and sphingolipids (see Ref. [43] and therein). Membrane rafts are, from a biochemical point of view, structures which resist solvation by detergents at low temperatures. Within the biophysical view, interactions between the highly saturated acids impose increased orientational ordering. Fatty acids within the rafts have limited mobility with respect to the unsaturated fatty acids in other parts of the membrane. Dynamic accumulation of specific membrane constituents in rafts regulates the spatial and temporal dependence of signalization and transport.

There is a mutual dependence between structure and shape of membranes. Membrane constituents create the membrane geometry by laterally moving to membrane locations with favorable local curvature [44–46]. Membrane curvature is thus determined by the shape of the membrane

constituents (rafts) and their interactions. The curvature of rafts is determined by the accumulation of a specific type of constituent and may be different from the curvature of the surrounding more fluid membrane. Considering this interdependence, the fluid mosaic model can be further modified.

A simple model of cell plasma vesiculation poses that the shape of a cytoskeleton-free membrane segment is driven toward the shape of its maximal difference of two membrane layer areas. This is possible by the rearrangement of laterally mobile membrane molecules that due to their geometrical shapes favor a certain local membrane curvature. Observations indicate that membranes of released vesicles differ in composition to their parent cells, indicating that the rearrangement of membrane constituents occurs during budding [47]. Vesiculation can therefore be thought of as a process by which the cell membrane loses some substances. Spontaneous and continuous budding and vesiculation of cancer cells therefore alters the original cell's function while also changing the number of its components [48].

2.2 Anisotropic orientational ordering and topological defects

Within the fluid mosaic model, biological membranes often exhibit some kind of in-plane orientational order [49–51], which could occur due to anisotropic shape of membrane components, for example anisotropic proteins or lipids [52–58]. Typical representative of such membrane inclusions are for example anisotropic banana-like shaped BAR protein domains [59], which may, due to their nematic in-plane ordering [60], stabilize thin tubular membrane protrusions [61–63]. In highly curved parts of the membrane, orientational order can locally arise from the alignment of these anisotropic components [51,64]. Membrane orientational ordering has been observed also in giant unilamellar vesicles al low temperatures where lipid molecules are in the gel or in some other ordered phase [65]. Orientational order in membranes may occur also due to chiral membrane constituents [66,67] or due to self-organized filament networks [68]. Lipid bilayer, which is the main building block of biological membranes, is basically a thin liquid crystal film [49,69]. In-plane orientational ordering in membranes could occur also due to the tilt of lipid chains [67,70,71] relative to the surface normal. Tilted lipid bilayers tend to have both tilt and hexatic order [72]. Hexatic tilt order in lipid bilayers can possibly rationalize the textures observed in gel domains [73]. Orientational ordering in hexatic membranes

has been experimentally observed [73], proving the concept of anisotropic membrane elasticity and orientational ordering of membrane components [74].

In biological membranes possessing tangential (in-plane) orientational ordering, topological defects are often present. In such membranes, topological defects are in most cases unavoidable due to topological reasons [75,76]. Topological defects correspond to localized distortions in a relevant order parameter field. They are a source of relatively large local elastic penalties and they cannot be removed by local continuous transformations. At the origin of topological defects, the ordering field is melted [77,78]. Therefore, presence of topological defects might have a strong impact of systems properties. Topological defects might for example serve as nucleating sites for anomalous membrane structural growth [79]. In biological membranes possessing orientational order, membrane configurations could be affected by the presence of topological defects [49]. Topological defects could for example trigger significant biological processes, such as cell fission [80]. Furthermore, local membrane shape can be altered due to spontaneous aggregation of curvature-inducing nematogens even at low concentrations [81]. It was shown that the coupling between in-plane nematic order and membrane curvature on deformable membrane surfaces can lead to generation of point and line topological defects, which leads to the production of membrane tubes and branches [82,83].

In the following model, we will demonstrate that for appropriate conditions, topological defects might trigger the pinching-off of a spherical bud from the parent membrane (membrane fission) in membranes exhibiting in-plane nematic ordering. To demonstrate such a vesiculation process, we use a simple mesoscopic minimal model, which treats membranes as effectively two-dimensional (2D) systems [49,52,69]. Namely, membrane thickness is in general relatively small with respect to system's typical linear dimension. We take into account also in-plane nematic-like ordering in the membrane. We will study the impact of membrane curvature on the number and position of topological defects. Analogous systems represent nematic liquid crystalline shells, which are of great interest due to their potential for various future photonic applications [75,84–87].

2.3 Theoretical modeling of membrane vesiculation

We model a membrane as a homogeneous two-dimensional film (fluid) exhibiting in-plane nematic ordering. To mathematically describe the local

shape of the membrane surface, we introduce a curvature tensor [69,75,88,89]:

$$\mathbf{C} = C_1 \boldsymbol{e}_1 \otimes \boldsymbol{e}_1 + C_2 \boldsymbol{e}_2 \otimes \boldsymbol{e}_2, \tag{1}$$

where unit vectors $\boldsymbol{e}_1$ and $\boldsymbol{e}_2$ determine the directions of maximal and minimal surface curvature and C_1 and C_2 are the corresponding principal curvatures. Note that the Gaussian curvature $K = Det\ \mathbf{C} = C_1 C_2$ and the mean curvature $H = Tr\ \mathbf{C} = (C_1 + C_2)/2$ of the surface are invariants of $\mathbf{C}$, where *Det* and *Tr* label the *determinant* and *trace* mathematical operation [90]. To describe the bending energy density of a membrane, we use the Helfrich's isotropic spontaneous curvature model [69,91–95]:

$$f_b = \frac{\kappa}{2}(C_1 + C_2 - C_0)^2 + \overline{\kappa} C_1 C_2, \tag{2}$$

where κ is the membrane bending modulus, $\overline{\kappa}$ the saddle-splay modulus and C_0 the spontaneous curvature of the membrane surface. For a fixed surface topology, the second term in Eq. (2), integrated over the whole membrane surface, is a constant [76]. Therefore, κ is arguably one of the most important quantities characterizing lipid membranes [96–98]. Different experimental and computational measurements of the bending modulus κ are discussed in Refs. [96–98]. Note that Eq. (2) is a limiting case of a more general model for membrane bending energy, which takes into account also the anisotropic properties of different membrane components [46,99].

Membrane orientational ordering is studied within a simple 2D Landau-de Gennes type model, where the degree of ordering is represented by the tensor order parameter [75,89]:

$$\mathbf{Q} = \lambda(\boldsymbol{n} \otimes \boldsymbol{n} - \boldsymbol{n}_\perp \otimes \boldsymbol{n}_\perp). \tag{3}$$

here, $\boldsymbol{n}$ and $\boldsymbol{n}_\perp$ are the eigenvectors of $\mathbf{Q}$ corresponding to the eigenvalues λ and $-\lambda$ [74]. In this parametrization, $\boldsymbol{n}$ represents the nematic director field, which exhibits head-to-tail invariance, where $|\boldsymbol{n}| = 1$ and states $\pm\boldsymbol{n}$ are physically equivalent [77]. Locally, the normal orientation of the membrane is determined by $\boldsymbol{\nu} = \boldsymbol{n} \times \boldsymbol{n}_\perp$. In Eq. (3), the amplitude λ represents the degree of orientational order and is bound to lie on an interval $\lambda \in [0,\ 1/2]$. The upper bound $\lambda = 1/2$ corresponds to the maximal degree of order, where molecules are rigidly aligned along $\boldsymbol{n}$. On the other hand, the orientational order is lost when $\lambda = 0$. Therefore, the points on the surface exhibiting $\lambda = 0$ usually reveal the locations of topological defects, since at the core of topological defects the nematic director is not defined [74,75,90].

We express the free energy density associated with nematic in-plane ordering in the membrane in terms of invariants of $\mathbf{C}$ and $\mathbf{Q}$, where the orientational condensation term f_c and orientational elastic term f_e are given by Refs. [75,89,90]:

$$f_c = -\alpha\ Tr\mathbf{Q}^2 + \frac{\beta}{2}\left(Tr\mathbf{Q}^2\right)^2, \tag{4}$$

$$f_e = \frac{k_i}{2}|\nabla_s\mathbf{Q}|^2 + k_e\mathbf{Q}\cdot\mathbf{C}^2. \tag{5}$$

In the nematic phase, the condensation term (Eq. 4) enforces the equilibrium nematic ordering amplitude $\lambda_0 = \sqrt{\alpha/\beta}$, where α and β are positive material constants [90]. The orientational (anisotropic) elastic term (Eq. 5) is weighted by positive intrinsic k_i and extrinsic (deviatoric) k_e elastic constants [50,51,100–105]. In Eq. (5), $\nabla_s = (\mathbf{I} - \boldsymbol{\nu}\otimes\boldsymbol{\nu})\nabla$ stands for the surface gradient operator, where ∇ represents 3D gradient operator and $\mathbf{I}$ is the identity matrix [75]. In this work, we will take into account only the impact of intrinsic elastic term k_i on orientational ordering within biological membranes exhibiting nematic ordering. The characteristic material dependent length of the model is estimated by the nematic order correlation length, which can be expressed as [75,90]:

$$\xi = \sqrt{\frac{k_i}{\alpha}}. \tag{6}$$

The free energy functional of the membrane exhibiting nematic ordering is written as an integral of the sum of the membrane isotropic bending energy (Eq. 2), the orientational condensation term (Eq. 4) and the orientational elastic term (Eq. 5) [75,89,90]:

$$F_{\text{tot}} = \iint_{\zeta} (f_b + f_c + f_e)\mathrm{d}^2\boldsymbol{r}, \tag{7}$$

where $\mathrm{d}^2\boldsymbol{r}$ is an infinitesimal element of the membrane surface and the integration is carried out over the whole membrane surface ζ. In Eq. (7), we took into account only the most essential terms needed to describe the vesiculation process.

In the simulations presented in this review, we consider closed axisymmetric shapes exhibiting inversion symmetry. To generate such shapes, we define the shell profile curve, which is then rotated about the z-axis by an angle of $\varphi = 2\pi$. In the Cartesian coordinates ($\boldsymbol{e}_x$, $\boldsymbol{e}_y$, $\boldsymbol{e}_z$),

the position vector of a generic point on an axisymmetric surface is given as [88,90]:

$$\boldsymbol{r} = \rho(s)\cos\varphi\boldsymbol{e}_x + \rho(s)\sin\varphi\boldsymbol{e}_y + z(s)\boldsymbol{e}_z, \tag{8}$$

where $\rho(s)$ and $z(s)$ are variational parameters defining the coordinates of the profile curve in the (x,z)-plane, s stands for the arc length of the profile curve, and φ is the azimuthal angle (see also Fig. 2). Equilibrium membrane configurations (shapes and orientational ordering profiles) are determined by minimizing the total free energy (Eq. 7) for fixed values of membrane surface and volume. Further numerical details are described in Refs. [90,106,107].

Membrane fission processes can also be described within our theoretical model. We will demonstrate key stages of the topological defect driven vesiculation. An important geometrical parameter defining closed membrane shapes is their reduced volume $v = V/V_0$, where V stands for the volume of a closed membrane shape, and V_0 is the volume of a spherical

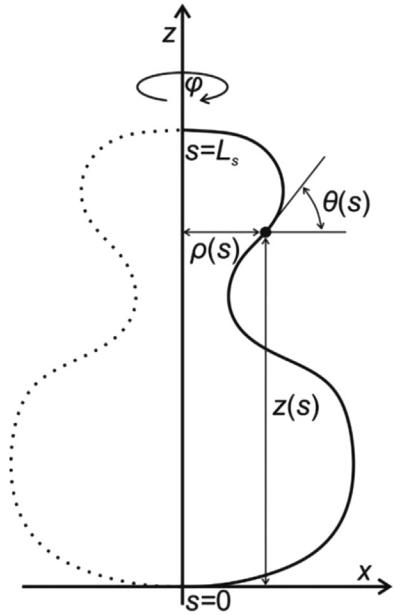

Figure 2 Shape profile curve in (x,z)-plane, where $\rho(s)$ is the radius and $z(s)$ the height of the shape profile at the given profile curve arc length s. Angle $\theta(s)$ represents the angle of the tangent to the profile curve with the plane that is perpendicular to the axis of rotation z. Profile curve of the length L_s is rotated around the z-axis by an angle of $\varphi = 2\pi$.

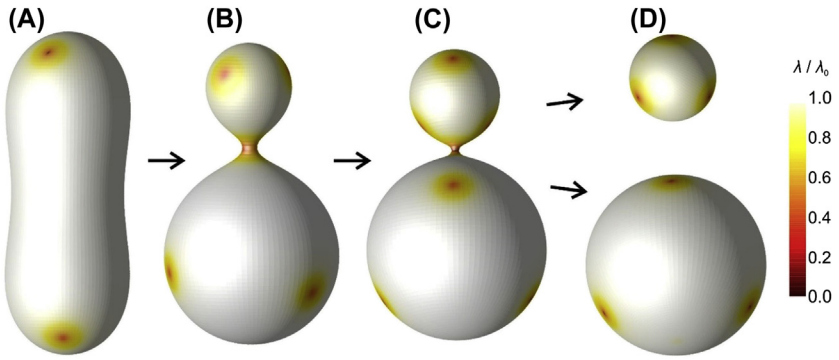

Figure 3 Orientational ordering profiles calculated on different closed membrane shapes. The shapes were calculated for: (A) $C_0 = 0$, (B) $C_0 = 2.5$ and (C) $C_0 = 4$. Other parameters for (A), (B) and (C) were set as: $v = 0.80$, $R/\xi = 14$, $k_e = 0$, $k_i \ll \kappa$. Two spherical shapes in (D) are formed as a results of decomposition of the shape in (C). Parameters were adjusted accordingly.

membrane of the same surface area and radius R [74]. Note that R represents a typical dimension of a shape, therefore, all lengths in the model are scaled with respect to R. In our simulations, we assume that a closed membrane shape undergoes a shape transformation from a prolate shape (Fig. 3A) to the shape with a thin neck (Fig. 3B and C). We enable this transformation by increasing the spontaneous curvature of the membrane C_0 (see Eq. 2). Spontaneous curvature is correlated to the curvature preferred by the membrane. In our simulations, C_0 is a dimensionless quantity scaled with respect to the typical linear dimension of the investigated closed surface R. Therefore, increasing C_0 can be seen as increasing the size of a closed membrane shape while keeping the non-scaled value of C_0 constant. With increasing the value of C_0 we actually simulate membrane growth (see Fig. 3).

Color plots in Fig. 3 and Fig. 4 represent the nematic ordering amplitude. At the core of topological defects, the nematic order is lost [75,88,90]. Therefore, topological defects are located at the points on the surface exhibiting $\lambda = 0$, which are marked with red color in Fig. 3 and Fig. 4. In Fig. 4, nematic ordering amplitude and nematic director field are shown in the (φ, s) plane where the positions of topological defects are clearly visible. According to the Gauss-Bonnet and Poincaré-Hopf theorems, topological defects are unavoidably formed on closed surfaces with spherical topology, where the total topological charge is given by $m_{tot} = 2$ [76,78]. In 2D systems, topological charge is equivalent to the

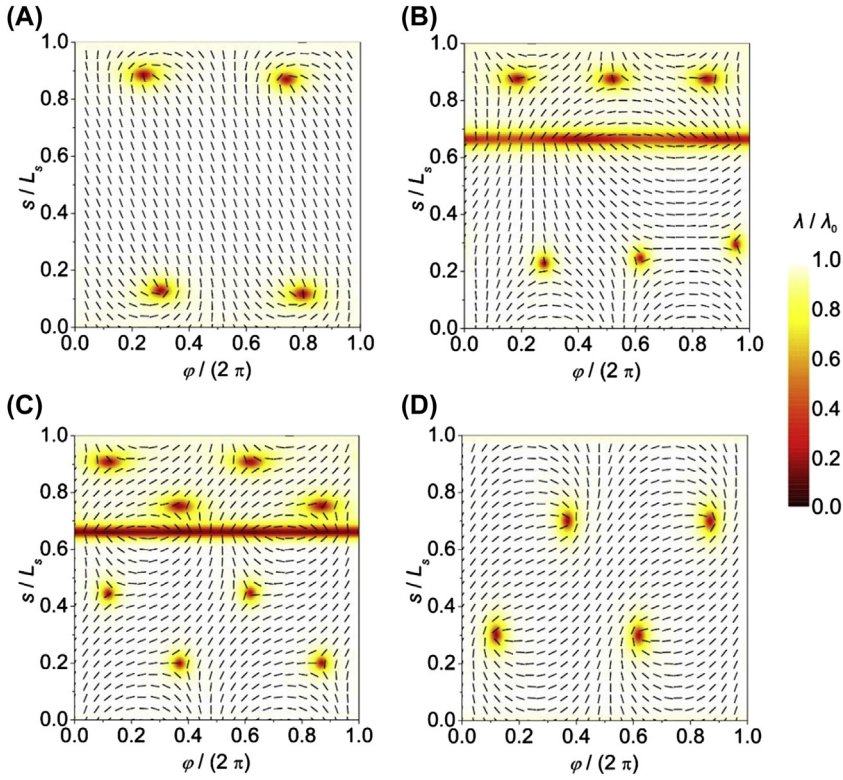

Figure 4 Superimposed nematic director field and the degree of orientational ordering in the (φ, s)-plane for the shapes presented in Fig. 3.

winding number, which is calculated as the total rotation of the orientational field divided by 2π on encircling the defect core counter clockwise [75,78,108].

Prolate shape (Fig. 3A and Fig. 4A) hosts four topological defects, which are located near the poles, where Gaussian curvature is relatively high. Each topological defect has a charge of $m = 1/2$, therefore, the total topological charge of the surface $m_{tot} = 2$, which is in agreement with the Gauss-Bonnet and Poincaré-Hopf theorems [76,78]. On increasing the spontaneous curvature C_0 of the membrane (which is equivalent to increasing the size of the closed surface at the constant value of non-scaled C_0), membrane shape transforms into the shape with a thin neck between two spherical parts (Fig. 3B). Such a shape hosts six topological defects of charge $m = 1/2$ and two topological antidefects of charge $m = -1/2$ (Fig. 3B and Fig. 4B), which gives $m_{tot} = 2$. Topological defects are located at two spherical parts

with positive Gaussian curvature, while the two antidefects are located within the neck, which exhibits negative Gaussian curvature (Fig. 3B and Fig. 4B). It was established that positive (negative) Gaussian curvature acts as an attractor for topological defects (antidefects) [79,90]. On further increasing C_0, the neck between the spherical parts becomes even thinner (Fig. 3C), which gives rise to the formation of additional pairs (defect, antidefect). Configuration on Fig. 3C and Fig. 4C possesses eight $m = 1/2$ topological defects (located at two spherical parts) and four $m = -1/2$ antidefects (located at the neck), yielding $m_{tot} = 2$. Note that the free energy of the structure shown in Fig. 3C and Fig. 4C is metastable with respect to the structure possessing six $m = 1/2$ and two $m = -1/2$ antidefects. Nevertheless, it is clear that on increasing C_0, antidefects are assembling within the neck of the closed membrane shape.

Topological defects are a source of large local elastic penalties. At the core of topological defects, the ordering field is melted and the degree of nematic ordering is relatively weak [77,78]. In our case, four topological antidefects are assembled within a relatively small neck region of the membrane (Fig. 3C and Fig. 4C). Consequently, local interactions between neighboring molecules within the neck are weakened, which might result in the neck rupture, leading to the fission (vesiculation) process [79]. In such a process, two distinct closed membranes are formed (see Fig. 3D). The final system (two spherical membranes) generally exhibits lower or the same membrane bending energy (Eq. 2) than the previous system (Fig. 3C). Spherical membranes (Fig. 3D) both host four $m = 1/2$ topological defects. Ordering profile on the bigger (lower) spherical membrane in Fig. 3D is plotted in Fig. 4D. Ordering profile on the smaller (upper) spherical membrane in Fig. 3D is similar, only defect cores are larger with respect to the shape size. This mechanism explains a possible membrane fission realization by taking into account the membrane elasticity theory and membrane orientational in-plane ordering.

We demonstrated a possible mechanism of membrane fission (vesiculation). Closed membrane shapes exhibiting spherical topology and in-plane ordering unavoidably possess topological defects [75,76]. In such membranes, regions with negative Gaussian curvature (narrow necks) could trigger the formation of pairs (defect, antidefect) [90]. We showed that antidefects assemble in the neck region of the membrane (Fig. 3B and C). Antidefects in the narrow neck induce relatively strong local fluctuations in orientational ordering, which weaken local intermolecular interactions. Consequently, this effect could enable rupture of the initial membrane

into two independent closed membranes (Fig. 3). Other possible membrane vesiculation mechanisms, for example the effect of area-difference elasticity and the effect of coupling of local lipid composition to Gaussian curvature are discussed in Refs. [109–111]. Note that in this contribution, we took into account only the so-called intrinsic term (see Eq. 5). In general, extrinsic (deviatoric) curvature terms are also present [50,51,100–105]. The extrinsic term (see Eq. 5) favors orientational ordering along the principal curvature direction with smaller curvature [90]. For the shapes considered in this review, the contribution of the extrinsic term would be largest within the neck region. The existence of in-plane ordering within narrow membrane necks was studied also within the so-called deviatoric elasticity model, which considers membranes with anisotropic components [51,112]. In these studies, it was established that the orientational ordering is increased within the neck, which implies that topological defects would assemble just above the neck, which does not qualitatively change the proposed membrane fission mechanism.

3. Biocompatible nanostructured materials for cancer diagnostic and therapy

Current cancer therapies are limited to surgery, radiation and chemotherapy. As all three methods risk damage to normal tissues or incomplete eradication of the cancer, it would be desirable to develop therapeutics that can either passively or actively target cancerous cells in their entirety. Nanomedicine is recently opening new avenues for cancer treatment with promise of significant breakthroughs in its diagnosis and monitoring [113].

In the past two decades, several therapeutics based on nanoparticles (NPs) in the size range 1–1000 nm have been successfully introduced for the treatment of cancer. It is anticipated that nanomaterials, which are molecular assemblies of functional chemistries, will be able to overcome biological barriers, accumulate in tumors and specifically recognize single cancer cells for detection and treatment [114]. These endeavors have led to experimenting with different types of nanomaterials with unique physical and chemical properties. However, in order for nanomaterials to be practical in clinical applications, the need for NPs to be multifunctional is immense and represents the epicenter of NP-treatment research [115]. Nowadays, design and development of multifunctional NPs – those that can perform many functions at once or sequentially, as needed – is one of the most important tasks in cancer research [116]. In the past few years different

varieties of multifunctional NPs have been developed, however, clinical application of most of them is limited due to their unwanted instability and cytotoxicity [115].

A combined approach which integrates therapeutics and diagnostics — commonly referred to as theranostics — is a new technological strategy to develop personalized cancer treatments with enhanced efficiency and safety [117]. Successful clinical applications of cancer theranostics require the discovery of tumor-homing multifunctional NPs, which can diagnose and deliver targeted therapy.

3.1 Photoactive nanoparticles for cancer treatment applications

With the progress of nanotechnology and nanomedicine in recent years, a new generation of engineered semiconducting nanomaterials have shown great promise as photosensitizers in photodynamic therapies (PDTs). The most important prerequisite for these materials is their capacity for reactive oxygen species (ROSs) generation at exposure to light [118]. It has been demonstrated that several photoactive inorganic semiconducting nanomaterials such as ZnO, TiO_2, Fe_2O_3, etc., can photo-generate ROS under illumination [119]. Among different semiconductors, titanium dioxide (TiO_2) is the most suitable photocatalytic material due to its high capacity for ROS photo-generation [120]. Titanium dioxide has been extensively studied for a number of versatile technological applications due to its inherent unique properties such as high chemical stability over a wide range of pH values, low cost, photo-activity, and excellent biocompatibility. Some applications of TiO_2 are in dye-sanitized solar cells, perovskite solar cells, air and water purification, antibacterial coating and photo-electrochemical water splitting. Recently, TiO_2 nanomaterials have been considered as a promising candidate in PDT as photosensitizer due to high potential for ROS photo-generation at exposure to UV-A, and biocompatibility in sub-illuminated conditions [121—123]. It has been reported that various ROS, such as superoxide ($O_2^{\bullet}$), singlet oxygen ($^1O_2$), hydroxyl radical ($^{\bullet}OH$), hydroperoxyl radical ($HO_2^{\bullet}$), and hydrogen peroxide (H_2O_2) are generated in a photocatalytic reactions on the TiO_2 surface upon light irradiation in aqueous solutions [124]. The photocatalysis of TiO_2 generally involves four stages: (i) generation of electrons and holes by photoexcitation; (ii) migration of the photo-generated charge carriers to the surface; (iii) subsequent reduction/oxidization of the adsorbed reactants, either directly by electrons/holes or indirectly by ROS; and (iv) recombination of the photo-generated

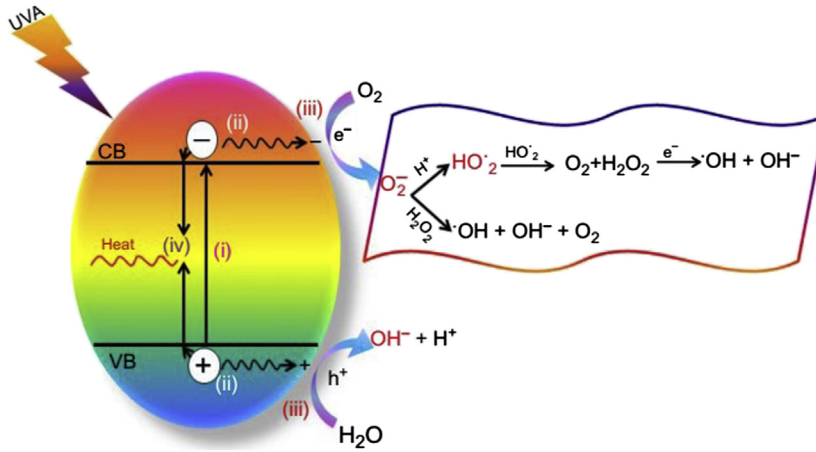

Figure 5 ROS generation through photocatalytic reactions of TiO_2 under UV-A irradiation: (i) generation of electrons and holes by photoexcitation; (ii) migration of the photo-generated charge carriers to the surface; (iii) subsequent reduction/oxidization of the adsorbed reactants directly by electrons/holes or indirectly by reactive oxygen species (ROSs); and (iv) recombination of the photo-generated electron-hole pairs [127].

electron-hole pairs. The desired photocatalysts are expected to promote processes (i), (ii), and (iii), and suppress process (iv) [125]. Fig. 5 schematically shows the photocatalytic reactions of TiO_2 under UV-A irradiation for ROS photo-generation [126].

The photo-killing activity of TiO_2 to malignant cells was first reported on a TiO_2 film electrode by Fujishima et al. [128]. Considering that the electrode system is not the most appropriate configuration for such application, water-soluble particulated TiO_2 — which could cover a larger effective surface area and can be incorporated inside cells — was applied for this purpose [129]. Under different experimental conditions using UV-A irradiation, various research groups demonstrated *in vitro* the phototoxic effect of TiO_2 nanoparticles (NPs) on a series of human cancer cells such as cervical cancer cells (HeLas) [130], bladder cancer cells (T24) [131], monocytic leukemia cells (U937) [132], adenocarcinoma cells (SPC-A1) [133], colon carcinoma cells (Ls-174-t) [134], breast epithelial cancer cells (MCF-7, MDA-MB-468) [135], glioma cells (U87) [136] and human hepatoma cells (Bel 7402) [137]. In the past decade, much research was dedicated to the photocatalytic destruction of cancerous cells with TiO_2 nanomaterials *in vitro* as well as *in vivo*, yet the practical use of TiO_2 as a photosensitizer in PDT for cancer destruction is still far from being put into practice [128,138,139].

The amount of photo-generated ROS by photosensitizer (exemplified here by TiO_2) represents an important factor in the photodynamic treatment of cancer cells. Any material used as a photosensitizer in PDT for cancer destruction should have the ability to photo-generate ROS in excess, well above the critical levels of ROS inside the cancer cells [140]. Therefore, the first step toward the practical use of TiO_2 as a photosensitizer in PDT for cancer destruction is the design of special types of water-soluble TiO_2 nanostructures with a high ROS photo-generation ability. Also important are photo-activation and a high degree of biocompatibility in the absence of light. It has been demonstrated that the geometry of TiO_2 NPs has a significant effect on their ROS photo-generation capacity. In particularly, the ROS photo-generation capacity is heavily dependent upon the surface chemical structure (the surface atomic arrangement and coordination) and topography, especially when particle size or nanostructured particle surface is reduced to the nanometer length scale, leading to a large specific surface area [141]. Based on this conviction, Seo et al. [142] successfully fabricated water-soluble TiO_2 NPs via a high-temperature non-hydrolytic method. When exposed to UV-A irradiation, these rod-shaped NPs (3.5 nm in diameter and 10.4 nm in length), exhibited higher photo-toxicity on human melanoma cells (A375) compared to commercially available Degussa P25 NPs [142]. With the aim of exploring the effects of nano-architecture on the control of intracellular ROS photo-generation and biocompatibility, a new type of particulated mesoporous TiO_2 microbeads (TiO_2 MBs), with a size greater than 100 nm, has been developed [143,144]. The TiO_2 MBs were synthesized via the solvothermal method; obtained MBs were monodispersed spheres with a diameter of 500 ± 50 nm and comparatively rough surfaces (Fig. 6) [145].

Judging from X-ray diffraction (XRD) experiments, the TiO_2 MBs exhibited very high crystallinity in the anatase phase [144]. The uniform contrast of the transmission electron microscopy (TEM) image from the edge to the center of a single sphere indicated that the entire TiO_2 MBs was composed of self-organized TiO_2 nanocrystals (constituent nanocrystals of MBs) with a high surface area and porosity (Fig. 7B and C) [146]. The constituent nanocrystals with different shapes adopted random orientations (Fig. 7D–F) [146], while a close examination of a single TiO_2 constituent nanocrystal by high-resolution TEM showed that they were completely crystalline along their entire lengths with the visible crystal lattice fringes.

Photocatalytic activity of TiO_2 MBs was evaluated in both biological environments for cancer cell destruction and out of the biological

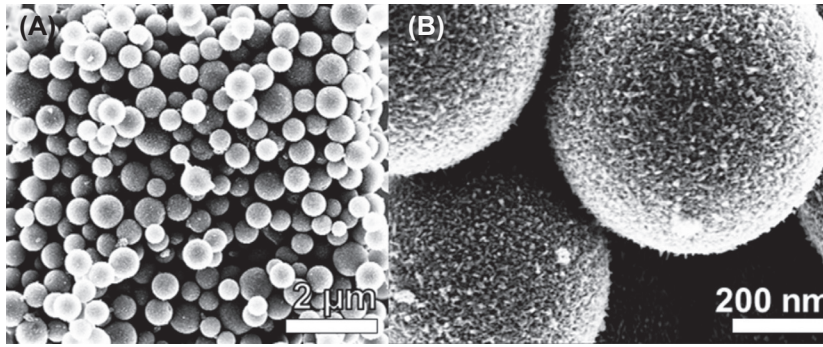

Figure 6 SEM images of TiO_2 MBs: (A) low-magnification SEM image of TiO_2 MBs and (B) high-magnification SEM image of TiO_2 MBs [145].

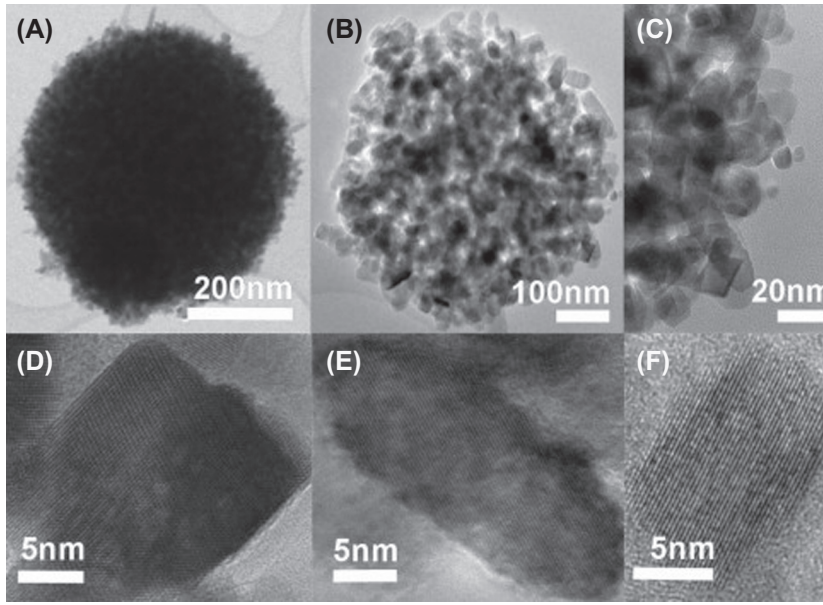

Figure 7 (A–C) TEM images of a single TiO_2 MB, (D–F) HRTEM images of constituent single nanocrystals (15 ± 5 nm) of anatase TiO_2 MBs with different sizes and shapes [146].

environments for directly oxidizing organic molecules [147]. Out of the biological environment and in identical experimental conditions, the photocatalytic activity of TiO_2 MBs was more than twice in comparison to commercial TiO_2 (P25 NPs) used for oxidization of 1,5-diphenyl carbazide (DPCI) to 1,5-diphenylcarbazone (DPCO). In the absence of

irradiation the cytotoxicity of TiO_2 MBs was assessed on a variety of normal and cancerous cells: healthy porcine urothelial cells (NPU), human low-grade urothelial cancer cells (RT4), human high-grade urothelial cancer cells (T24), prostate cancer cells (PC3s) and healthy embryonic fibroblast cells (MEF). *In vitro* cytotoxicity results showed the TiO_2 MBs, unlike TiO_2 nanoparticles, are exceptionally biocompatible with all type of tested cells in the absence of irradiation [131,147,148]. Based on numerous examples provided by Wiesner's group, the optimal safe size was shown to be around 100 nm, below which atypical surface reactivity arises and causes usual nano-scale toxicity [149]. The high degree of biocompatibility of TiO_2 MBs in the absence of irradiation might be attributed to the size and architecture of MBs. Under identical photo-activation, TiO_2 MBs showed higher photocatalytic activity for prostate cancer cells (PC3s) destruction compared to TiO_2 NPs. Upon on/off-switchable photo-activation with UV-A, the TiO_2 MBs had delivered significant anticancer effects by enhancing the intracellular ROS level and thus reducing the survival of cancer cells by at least six times more than TiO_2 NPs [147]. An efficient method for full removal of high-grade urothelial cancer cells based on TiO_2 MBs photocatalysis was proposed by Imani et al. [131]. In clinical practice the main problem in treating bladder cancer is not how to eliminate the main population of cancer cells, but rather the accessibility of drugs to the remaining cancer cells, as they represent seeds for new urothelial tumors [150,151].

With conventional cancer treatments, the remaining cancer cells are kept within healthy urothelial tissue, where they are protected from chemotherapeutic drugs by the tight blood-urine barrier provided by healthy urothelial cells (Fig. 8A) [131]. Such persisting cancer cells are thought to be responsible for the relapse of bladder tumors [150,152]. In order to nullify these hidden cancer cells, an essential prerequisite in the first step is to remove the superficial layer of differentiated urothelial cells (umbrella cells; see Fig. 8B) [131]. To overcome this problem, Imani, and et al., have proposed a combination of 1 min UV-C pre-treatment to remove the superficial layer of differentiated urothelial cells and TiO_2 MBs photocatalytic treatment for destruction of hidden cancer cells. In the suggested method, high-grade urothelial cancer cells (T24) were subjected to UV-C irradiation for 1 min, successfully removing superficial cells, while longer wavelengths (e.g., UV-A) failed to remove these cells [131]. In the second step, the biocompatible TiO_2 MBs were introduced into high-grade urothelial cancer cells to be internalized (Fig. 8C) [131]. Next, the urothelial cancer cells containing TiO_2 MBs were exposed to irradiation. Since the energy for ROS

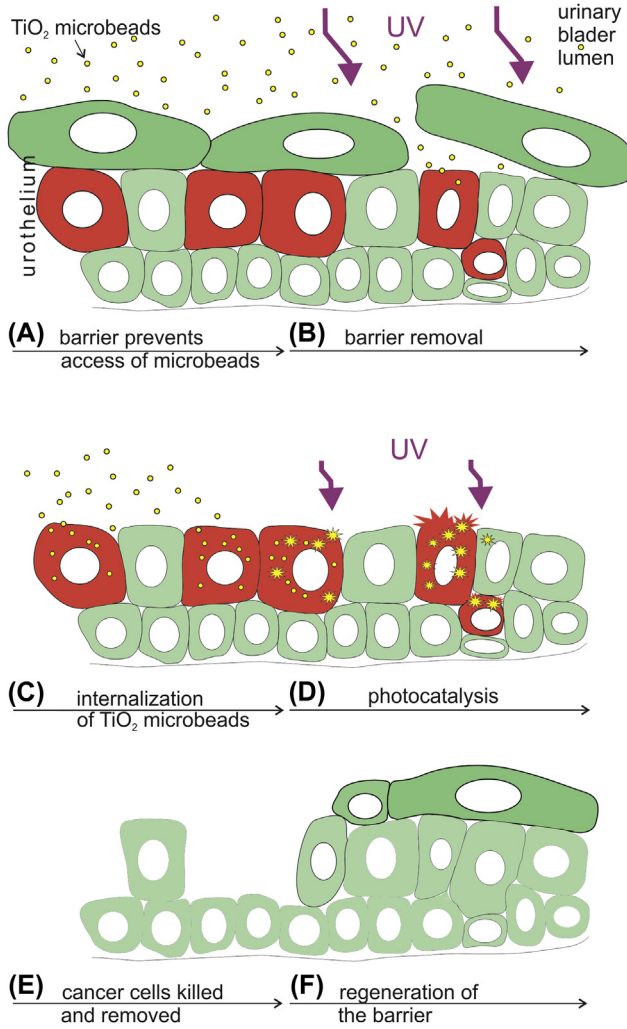

Figure 8 Scheme of the proposed supplemental treatment of the *in vivo* urinary bladder cancer cells by a combination of UV-irradiation and TiO_2 MBs. Legend: red – cancer cells, green – healthy urothelial cells (dark green depicts differentiated urothelial cells), purple – UV-irradiation (smaller arrows in D) depict irradiation with reduced intensity or one with less-energy in comparison to A) [131].

photo-generation through TiO_2 MBs photocatalysis for UV-A is lower than the one needed for the removal of umbrella cells (UV-C), one might reduce the intensity of UV-C irradiation to harm only cancer cells or use only UV-A irradiation [131]. Finally, the regeneration and differentiation of the remaining healthy urothelial cells could restore the urothelium and its

blood-urine barrier function (Fig. 8F) [131]. A remarkably rapid regeneration of the urothelial tissue was observed within the hour, preventing unfavorable effects of barrier removal and the potential toxic effects on regenerating healthy cells, caused by UV-C irradiation [131]. It is thus possible this strategy could selectively kill cancer cells containing TiO_2 MBs, but preserve healthy cells in the urothelium [131]. It has been proven that less differentiated cells have a highly increased potential for endocytosis in comparison to normal urothelial cells, giving a strong emphasis on the selectivity of this suggested treatment [153]. Furthermore, the enhanced phototoxicity of UV-C irradiation in cells that have endocytosed TiO_2 MBs works in favor of the selective treatment of exposed cancer cells after the removal of the umbrella cell shield by UV-C irradiation (Fig. 8D and E) [131].

It is of great importance that the increased ROS generation all over the body is avoided to prevent damage to healthy cells. In this regard, the monitoring and tracking of TiO_2 MBs concentrations in cell tissues around the cancerous cells before and during irradiation are vital [154,155]. Unfortunately, TiO_2 alone does not have any useful properties to be monitored directly inside the body. Furthermore, any modifications with appropriate surface-capping ligands would reduce its ROS photo-generation efficiency [156]. The future implementations of TiO_2 MBs in photodynamic therapies therefore depend heavily on modification of TiO_2 MBs to gain multifunctional particles with maximum imaging and therapeutic capacities. This feat entails a compromise between ROS photo-generation, endocytosis, and low toxicity to surrounding healthy cells. The addition of imaging agents into TiO_2 MBs, such as various contrasts, is crucial for ensuring reliable particle tracking and delivery. Among different imaging methods, optical imaging (OI) has the greatest resolution for visualizing subcellular structures [157], while magnetic resonance imaging (MRI) has the advantage of being minimally invasive and can be used to obtain clear contrast for many soft tissues [158]. The combination of MRI and OI in one MRI−OI probe is thus a useful tool for medical imaging, and combined MRI−OI agents have great application potential in selective tumor labeling for oncological diagnosis and surgery [159]. In the past decade, different types of nanocompounds as imaging agents have been developed [160]. Among these imaging agents the lanthanide nanocompounds (often collectively known as the rare earth (RE) elements) have attracted considerable attention as medical imaging probes [161], in particular gadolinium (Gd) compounds. Paramagnetic gadolinium (III) ions (Gd^{3+}) contain seven unpaired electrons that can

efficiently alter the relaxation time of surrounding water protons and have been widely used in routine clinical imaging as MRI contrast agents in hospitals [162]. Many efforts have been devoted to explore TiO_2 based phosphors with various RE dopants [163]. Based on these concepts, scientists have speculated that with the proper incorporation of Gd (RE elements) to TiO_2 lattice structure, titania with MRI-OI functionality could be obtained.

Recently, Imani et al. reported on gadolinium-doped TiO_2 nanobeads (TiO_2@Gd NBs) that exhibit simultaneous OI-MRI properties as well as enhanced ROS photo-generation capacities [8]. Multifunctional TiO_2@xGd NBs (here, x denotes the gadolinium molar ratio: 0, 5, 10, 15, 20%) were synthesized via a solvothermal method that was similar to the procedure used in the production of TiO_2 MBs. The only difference in the process was the addition of dopant gadolinium (III) nitrate hexahydrate to the precursor solution. Morphological and structural characterization of these TiO_2@xGd NBs revealed the formation of monodispersed mesoporous spheres in anatase phase only for un-doped TiO_2 NBs, TiO_2@5%Gd NBs, and TiO_2@10%Gd NBs (Fig. 9) [8].

A comparative study of photocatalytic activities and imaging functionality of TiO_2@xGd NBs and commercial P25 has been conducted by Imani et al., to explore how nanoscale doping switches the ROS photo-generation and imaging functionality of TiO_2@xGd NBs. The results of photocatalytic experiments demonstrated that ROS photo-generation capacities of TiO_2@xGd NBs doped with low concentrations of Gd (5% Gd and 10% Gd) were significantly increased compared to un-doped TiO_2 NBs and P25. Highest photocatalytic activity was observed for TiO_2@10%Gd. Increase in doping concentrations (15% and 20% Gd) significantly reduced the ROS photo-generation capacities, even in comparison to undoped TiO_2 NBs and P25 [164]. These findings indicate that only TiO_2@xGd NBs doped with low concentrations of Gd (5% Gd and 10% Gd) are promising photosensitizer agents in PDT for destruction of cancer cells. According to photoluminescence (PL) spectroscopy results, all of the doped TiO_2@xGd NBs exhibited red emission at 637 nm upon UV excitation that is beneficial for OI. An increase in Gd doping resulted in an increased emission intensity and decreased photocatalytic activity with maximum emission observed at TiO_2@15%Gd [165]. To investigate how Gd^{3+} doped TiO_2 NBs would function as a contrast agent in MRI, the relaxation times (T_1, T_2) of TiO_2@*x*Gd NBs were measured in a static magnetic field at 400 MHz. Both the spin–lattice relaxation time (T_1) and the spin–spin relaxation

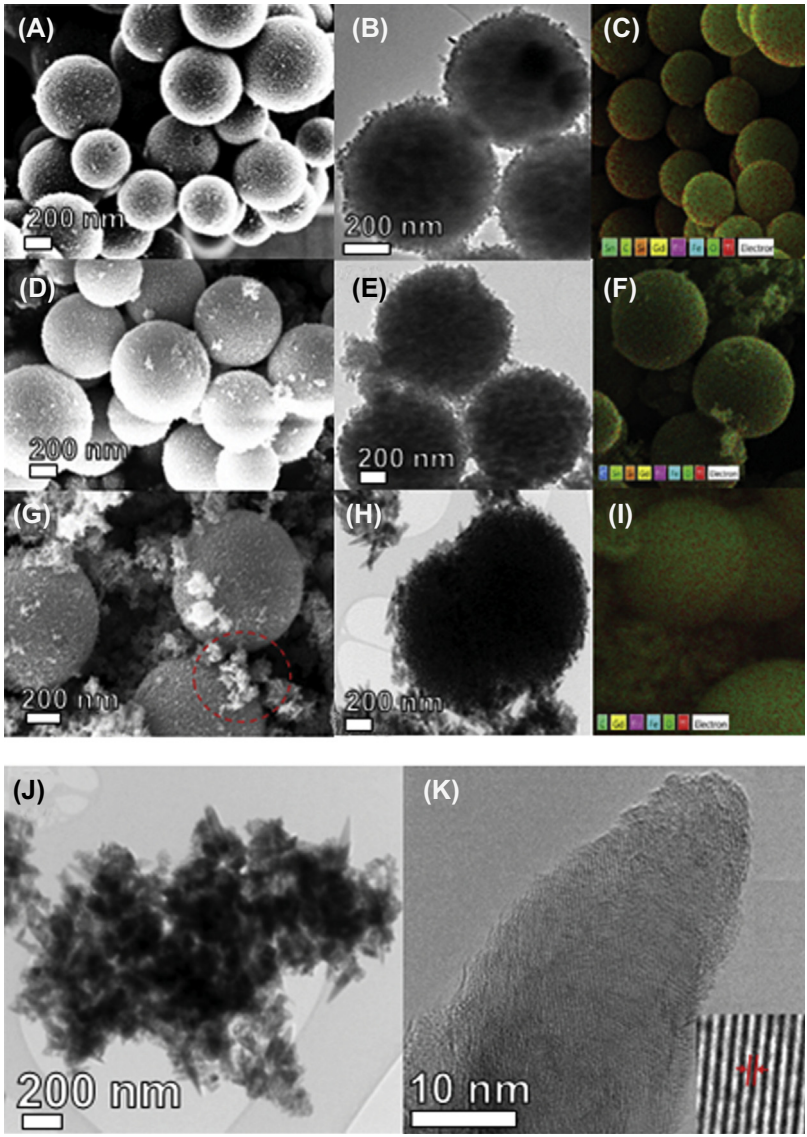

Figure 9 SEM (A, D, G), TEM (B, E, H), and EDS (C, F, I) images of obtained NP structures: TiO_2 NBs (A—C), TiO_2@5%Gd NBs (D—F) and TiO_2@10%Gd NBs (G—I); red circle indicating the nano-star clusters in TiO_2@10%Gd NBs. (J) TEM, and (K) HRTEM images of nano-star clusters, the crystalline plane of the nanoparticle is shown in (K) [8].

time (T_2) were shortened for Gd^{3+}-doped TiO_2 NBs in comparison with un-doped TiO_2 NBs. Moreover, relaxation rates $R_1 = 1/T_1$ and $R_2 = 1/T_2$ expressed as millimolar relaxivities r_1 and r_2 were increased significantly with increased Gd amount and highest relaxivity was recorded for TiO_2@15%Gd NBs, same as for PL emission. The relaxivity recorded for the TiO_2@15%Gd NBs was surprisingly high ($r_2 = 126\ mm^{-1}\ s^{-1}$) compared to a commonly available contrast agent, and thus showed promising clinical use. The T_1 shortening effect of TiO_2@10% Gd NBs was moderate ($r_1 = 4.7\ mm^{-1}\ s^{-1}$); however, T_2 shortening effect of this sample was high ($r_2 = 80\ mm^{-1}\ s^{-1}$), where r_2 relaxivity of TiO_2@10% Gd NBs was even a few times greater than for clinically available contrast agents [158].

In vitro cytotoxicity of TiO_2@*x*Gd NBs added to MG-63 cells in the absence of irradiation was tested and the cell viability results confirmed that TiO_2@*x*Gd NBs are fully biocompatible for all tested concentrations [8,145]. Furthermore, *in vitro* test results showed that attachment to cell surfaces and internalization was greater for TiO_2@*x*Gd NBs in comparison with un-doped TiO_2 NBs (Fig. 10) [8]. In cancer treatment, cellular internalization of anticancer-imaging agents is an important requirement for effective and safe PDT with a selective delivery of anticancer-imaging agents into cancerous cells [166]. Multifunctional TiO_2@*x*Gd NBs showed significant cellular internalization and passive accumulation inside cancerous cells, demonstrating a possible method for selective ROS photo-generation inside cancerous cells without damage to healthy cells.

In addition, *in vitro* tests were performed where MG-63 cells incubated with TiO_2@*x*Gd NBs were irradiated with UV-A for varying amounts of time. Viability test result showed that just after 3 min of irradiation, TiO_2@*x*Gd NBs delivered their ROS photo-generation potential for removal of all cancerous cells. After 3 min of UV-A irradiation, architectural TiO_2@10%Gd NBs – compared to un-doped TiO_2 NBs and TiO_2@5%Gd NBs – demonstrated highest anticancer effects by enhancing the intracellular ROS level and reducing the survival of MG-63 cells (Fig. 11) [8].

According to research results by Imani et al., TiO_2@10%Gd NBs could be introduced as a promising platform for simultaneous cancer cell imaging and treatment by PDT. The TiO_2@10%Gd NBs form a fully biocompatible

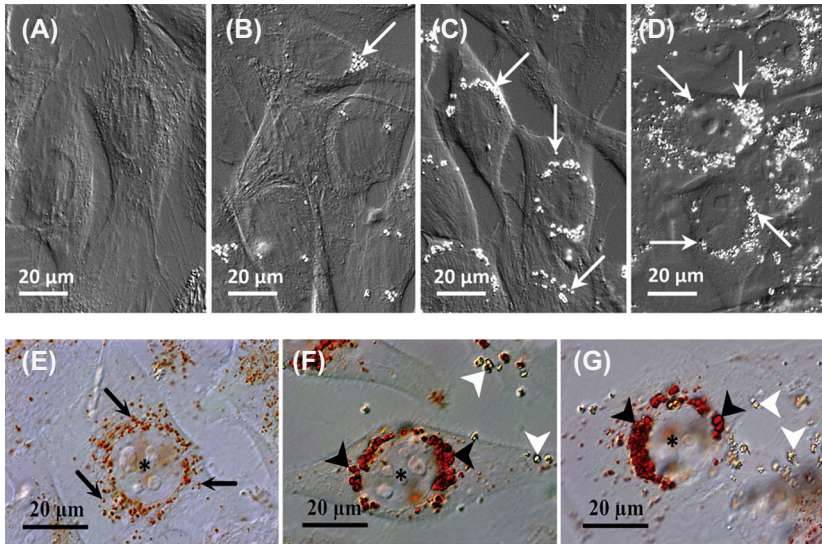

Figure 10 MG-63 cells treated with TiO_2@xGd NBs (A—D). Differential interference contrast (DIC) *images* of MG63 cells after 1-h incubation with 50 μg/mL NBs: (A) untreated control cells, (B) cells treated with TiO_2 NBs, (C) cells treated with TiO_2@5% Gd NBs, (D) cells treated with TiO_2@10%Gd NBs; arrows are showing NBs. Acid organelles in MG-63 cells treated with TiO_2@xGd NBs (E—G). Differential interference contrast (DIC) *images* of MG-63 cells after 1-h incubation with 50 μg/mL NBs: (E) untreated control cells, (F) cells treated with TiO_2@5%Gd NBs, (G) cells treated with TiO_2@10%Gd NBs and additional 24 h incubation. Acid organelles are stained red by Neutral red dye. In untreated control cell (E) acid organelles are small and round shape (arrows). In TiO_2@ 5%Gd NBs (F) and TiO_2@10%Gd NBs treated cell (G) acid organelles are bigger and irregular shape (black arrowheads). Shape of red acid organelles is similar to un-internalized, unstained NBs (white arrowheads). Cell nuclei are marked with asterisk [8].

system for OI-MRI and selective ROS photo-generation inside the cancer cells, providing impressive multifunctionality and allowing simultaneous OI-MRI and PDT without the need to compromise the advantages of either component. Furthermore, TiO_2@10%Gd NBs showed significant cellular internalization and passive accumulation inside cancerous cells, providing a safe manner for selective ROS generation inside the cancerous cells without collateral damage to healthy cells.

However, if medical imaging capabilities PDT are needed, the TiO_2@ 15%Gd NBs with maximized PL intensity, quite high T_1 shortening effect and relaxivity being a few times greater than in commercial materials would be promising for use as efficient and fully biocompatible OI-MRI contrast agent [158].

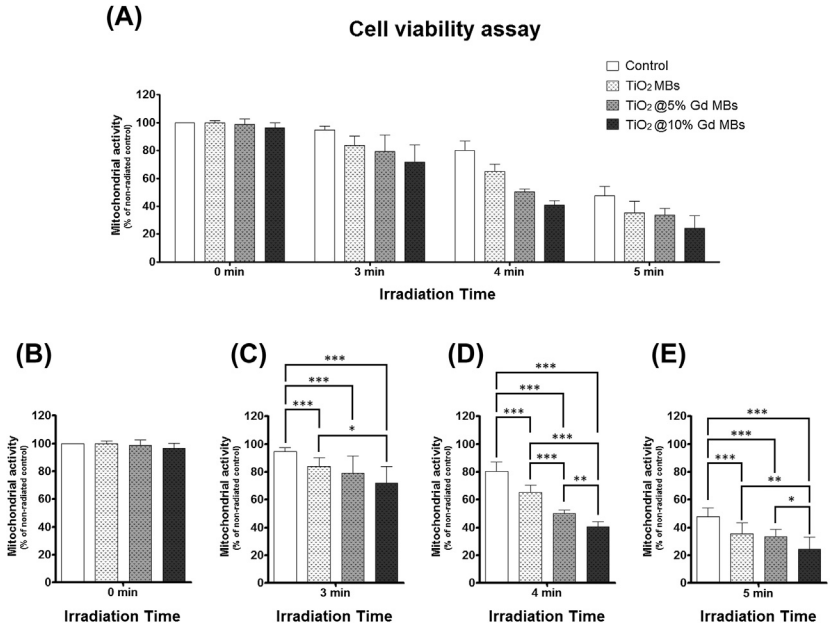

Figure 11 Cell viability of MG-63 cells after 1-h exposure to TiO_2@xGd NBs followed by UV-A radiation and 24-h post-incubation, tested by resazurin assay. Results are presented as the mean (+SD) percentage of untreated, non-radiated control in the experiment performed twice in at least five replica wells. Asterisks in the lower graphs (B–E) denote the significant differences between samples (*$p < 0.05$; **$p < 0.01$; ***$p < 0.001$; Student's *t*-test). Cell viability between non-radiated samples (0 min) treated with TiO_2@Gd NBs, did not significantly differ in comparison to untreated control [8].

4. Nanoparticle encapsulation

It has been demonstrated cellular internalization directly is linked to physical properties of the cell membrane [9], and precise tailoring of physical properties of cell membrane is essential for development of multifunctional particles with selective internalization in cancerous cell. The cellular internalization usually consists of two processes, adsorption on the membrane, and internalization by endocytic or non-endocytic (diffusion through membrane) pathways [167].

NBs and macromolecules are usually taken up into cells through endocytosis, which is thought as a fundamental and energy costing process. When NBs adsorbs on a flexible membrane due to a local adhesion potential, the membrane deforms and wraps around the NBs and consequently engulf the

NBs [168,169]. The wrapping of NBs by a membrane is related to the budding of vesicles [170,171], and plays an important role is NB internalization. To understand the physics and dynamics of these processes, which all involve elastic membrane deformations, we must understand the physical properties of the cell membrane. It is desirable to have a better understanding of how physical parameters of membrane like bending stiffness, lateral tension or adhesion strength control the wrapping and internalization. Many modern experimental techniques directly probe the physical properties of the cell membrane before and after NP internalization. However, experimentally systematic visualization of dynamic deformation of membrane during NP internalization is to date impossible to observe. Computational methods, including theoretical calculations and computer simulations, on the contrary, may offer precise information for the dynamic deformation of membrane and NP internalization [172]. Since computational methods allow for investigations of these systems at the molecular level, they have great potential for determination of regimes of bending rigidity, surface tension, intrinsic lipid curvature, and effective receptor binding energies that lead to efficient wrapping and maximum endocytosis [9].

4.1 Monte Carlo simulations of particle encapsulation

The theoretical interactions between a cellular membrane and colloidal particles have been studied extensively in the past, simulating various mechanisms of interaction. Deserno and others analyzed the wrapping of colloids by membranes in the presence of a short-ranged adhesive interaction potential [173,174]. The deformation of an initially flat membrane is in this case determined by both, the bending energy and interfacial tension, predicting a discontinuous transition from a partially to fully wrapped bound state. If the membrane is simulated in a way that includes a mixture of opposite spontaneous curvatures, encapsulation will be aided by local lipid demixing [169]. In another study using a nonlinear Poisson-Boltzmann model of adhering charged proteins, the demixing of binary charged lipids of an initially planar membrane will be induced by the proteins' charge, defining a wrapped transition state only above some critical protein charge [175]. In general, the encapsulating transitions are discontinuous in nature.

Here we review a method utilizing a Monte Carlo approach to electrostatically driven colloid adhesion and wrapping of a charged spherical colloid by a fluid binary vesicle [170]. The surface of the vesicle is randomly triangulated with charges that can move laterally within the lattice. The mobile charges are opposite in sign to the fixed colloid charges and the electrostatic

interaction is described by the linear Debye-Hückel potential. Interaction of the colloid with the vesicle is optimized by both, changing of shape and charge distribution. A minimal phenomenological model of free energy minimization complements the simulations and correctly predicts the discontinuity of the wrapping transition [170].

In the Monte Carlo approach the vesicle is represented by a set of $N = 1447$ vertices that are linked by tethers of flexible length to form a closed, randomly triangulated and self-avoiding network. Membrane fluidity is maintained by flipping bonds within the triangulated network. A single bond flip of the four vertices of two neighboring triangles consists of cutting the tether between two connected vertices and reestablishing it with the previously unconnected two vertices. A Monte Carlo step involves of random bond flips and random perturbations of positions of the vertices in 3D space, allowing for their redistribution for any given vesicle shape. The interaction of the charged colloid with the vesicle is then optimized with respect to both the vesicle shape and distribution of charged vertices. The total energy H of a given microstate of the colloid and vesicle system is given by the sum of their bending and electrostatic energies [170]:

$$H = \frac{\kappa}{2}\int_A ds(c_1 + c_2)^2 + \frac{kT}{2}\sum_{i,j} u\left(\left|\boldsymbol{r}_i - \boldsymbol{r}_j\right|\right). \tag{9}$$

here, the first part of the total energy is the bending energy of the membrane, with κ being the bending stiffness and $c_1 + c_2$ the sum of the two principal curvatures integrated over the entire surface of the closed vesicle. The second term is the electrostatic contribution of all elementary charges located at direct positions $\boldsymbol{r}_i$ and $\boldsymbol{r}_j$. The electrostatic contribution of the colloid is constant and can therefore be omitted. Thermic energy is denoted by kT. In some cases, the mobile charges are assigned a preferred spontaneous curvature, adding another component to the total energy H [170]:

$$-c_0\kappa\int_A ds\eta(c_1 + c_2), \tag{10}$$

where η denotes the charge of a given vertex corresponding to a lateral area. For a more detailed account of derivations and numerical simulations, see Ref. [170]. The Monte Carlo simulations of microstates are sampled according to the Metropolis algorithm, where the evolution of the system is measured in millions of Monte Carlo steps. One such step consists of

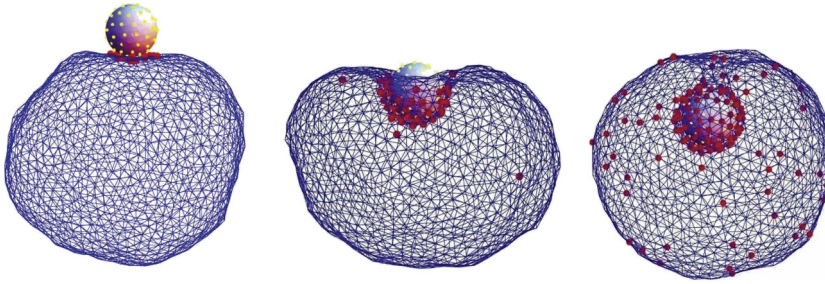

Figure 12 Monte Carlo simulations of wrapping of a spherical, oppositely charged colloid by a triangulated model membrane. The red dots represent the mobile charges that can move laterally between the vertices. From left to right, the number of mobile charges on the vesicle is increasing ($M = 15$, 60 and 150) in proportion of increased wrapping of the colloid. *Adapted from M. Fošnarič, A. Iglič, D.M. Kroll, S. May, Monte Carlo simulations of complex formation between a mixed fluid vesicle and a charged colloid. J. Chem. Phys. 131 (10) (2009) 09B610.*

separate displacements of each of the N vertices by a random increment in the cube followed by N attempts to flip a randomly chosen bond. The number of charged vertices is given by M.

We can see a number of typical conformations of the vesicle-colloid system in Fig. 12 as obtained by the Monte Carlo simulations in dependence on the number of mobile charges on the vesicle. The figures of Monte Carlo simulations indicate a relation between the degree of wrapping (denoted by the degree of wrapping λ; for details, see Ref. [170]) and charge segregation on the surface of the vesicle. For $M = 15$, all charges on the vesicle are screened close to the colloid (left snapshot in Fig. 12). The colloid is adsorbed to the vesicle despite a small degree of wrapping ($\lambda = 0.15$). At $M = 60$, when the charge is about half that of the colloid, we observe total charge segregation and a wrapping parameter $\lambda = 0.5$. Some charges can escape the warped region of the membrane due to thermal fluctuations. For $M = 150$, the vesicle charge overcompensates that of the colloid leading to a complete engulfment, as seen in Fig. 12.

It is found that the number of charged vertices in the wrapping region changes continuously, while the total engulfment of the colloid (endocytosis) is coupled to the lateral separation of the mobile charges on the surface of the vesicle. As is predicted for colloids interacting with the membrane by a short-ranged adhesive potential [173,174,176], the investigated system exhibits a discontinuous wrapping transition from partially to fully wrapped. Decreasing the bending stiffness of the vesicle weakens the wrapping transition. The wrapping transition shifts to smaller ratios of M/N if the charged

vertices possess a spontaneous curvature that matches the curvature of the colloid. In the opposite case, however, the wrapping is a continuous process and the preferred shape of the vesicle becomes non-axisymmetric [170].

The discussed model demonstrates a fundamental process of endocytosis, relevant not only for further studies of cancer treatment of TiO_2@xGd NBs, but also in viral budding and various biotechnological applications. The spherical colloid in the model represents a charged nanoparticle, while the mobile charge constituent on the membrane surface may simulate lipids, glycolipids or proteins. Investigating the nature of wrapping transitions could potentially lead to an optimization of NB functionality, including its physical properties such as doping, which directly translate to charge distributions within the nanoparticles.

5. Conclusions

In this review, we revised two emerging mechanisms of cancer diagnostics and treatment, subsequently presenting two respective and rigorous biophysical approaches that aim to improve their understanding.

First, we have looked at the correlations between cancer and extracellular vesicles and went on to discuss the physical modeling of cellular membrane vesiculation within the fluid mosaic model. We have demonstrated that the consideration of anisotropy in biological membranes, characterized by the orientational ordering of membrane rafts with preferable spontaneous curvature, can lead to topological defects, leading to regions of negative Gaussian curvature. These regions of strong orientational ordering form within narrow necks and can potentially lead to the formation of pairs, simulating the budding and separation of extracellular vesicles observed in cells. The model is promising in cancer diagnostics and shows potential use in the mechanisms of biomarkers.

Secondly, we reviewed a recent nanoparticle therapy of gadolinium doped mesoporous TiO_2 nanobeads, which show promise as biomarkers as well as therapeutic agents. The discussed particles have high stability and biocompatibility, while simultaneously providing impressive multifunctional properties for optical and magnetic resonance imaging as well as photodynamic therapy. Through evidence of particle engulfment by the cancerous cells, we have revised a numerical Monte Carlo model of endocytosis that simulates the engulfing of an oppositely charged particle by minimizing the free bending energy and electrostatic potential of a model

cell. With the inclusion of laterally mobile charges within the triangulated mesh of the vesicle, we have seen that the wrapping transition depends on the strength of mobile charges. Such insight could lead to functional optimization of nanoparticles for maximum cell intake and therapy purposes.

Acknowledgements

This review article was supported by the Slovenian Research Agency (ARRS) grants Nos. J5-7098, P3-0388, P2-0232 and L7-7566 and grant H2020 VES4US. We would also like to acknowledge Dr. Metka Benčina and Dr. Tina Mavrič. The grant VES4US was financed by EU Commission.

References

[1] S. Fais, L. O'Driscoll, F.E. Borras, E. Buzas, G. Camussi, F. Cappello, J. Carvalho, A. Cordeiro da Silva, H. Del Portillo, S. El Andaloussi, Evidence-based clinical use of nanoscale extracellular vesicles in nanomedicine, ACS Nano 10 (4) (2016) 3886−3899.

[2] M. Manček-Keber, M. Frank-Bertoncelj, I. Hafner-Bratkovič, A. Smole, M. Zorko, N. Pirher, S. Hayer, V. Kralj-Iglič, B. Rozman, N. Ilc, Toll-like receptor 4 senses oxidative stress mediated by the oxidation of phospholipids in extracellular vesicles, Sci. Signal. 8 (381) (2015) ra60.

[3] E. Ogorevc, V. Kralj-Iglic, P. Veranic, The role of extracellular vesicles in phenotypic cancer transformation, Radiol. Oncol. 47 (3) (2013) 197−205.

[4] M. Yáñez-Mó, P.R.-M. Siljander, Z. Andreu, A. Bedina Zavec, F.E. Borràs, E.I. Buzas, K. Buzas, E. Casal, F. Cappello, J. Carvalho, Biological properties of extracellular vesicles and their physiological functions, J. Extracell. Vesicles 4 (1) (2015) 27066.

[5] F. Grizzi, M. Chiriva-Internati, Cancer: looking for simplicity and finding complexity, Cancer Cell Int. 6 (1) (2006) 4.

[6] D. Sweeton, S. Parks, M. Costa, E. Wieschaus, Gastrulation in Drosophila: the formation of the ventral furrow and posterior midgut invaginations, Development 112 (3) (1991) 775−789.

[7] S. Letoffe, J. Ghigo, C. Wandersman, Iron acquisition from heme and hemoglobin by a *Serratia marcescens* extracellular protein, Proc. Natl. Acad. Sci. Unit. States Am. 91 (21) (1994) 9876−9880.

[8] R. Imani, R. Dillert, D.W. Bahnemann, M. Pazoki, T. Apih, V. Kononenko, N. Repar, V. Kralj-Iglič, G. Boschloo, D. Drobne, Multifunctional gadolinium-doped mesoporous TiO_2 nanobeads: photoluminescence, enhanced spin relaxation, and reactive oxygen species photogeneration, beneficial for cancer diagnosis and treatment, Small 13 (20) (2017) 1700349.

[9] Z.G. Qu, X.C. He, M. Lin, B.Y. Sha, X.H. Shi, T.J. Lu, F. Xu, Advances in the understanding of nanomaterial−biomembrane interactions and their mathematical and numerical modeling, Nanomedicine 8 (6) (2013) 995−1011.

[10] V. Muralidharan-Chari, J.W. Clancy, A. Sedgwick, C. D'Souza-Schorey, Microvesicles: mediators of extracellular communication during cancer progression, J. Cell Sci. 123 (10) (2010) 1603−1611.

[11] A. Janowska-Wieczorek, L.A. Marquez-Curtis, M. Wysoczynski, M.Z. Ratajczak, Enhancing effect of platelet-derived microvesicles on the invasive potential of breast cancer cells, Transfusion 46 (7) (2006) 1199−1209.

[12] J.-K. Lee, S.-R. Park, B.-K. Jung, Y.-K. Jeon, Y.-S. Lee, M.-K. Kim, Y.-G. Kim, J.-Y. Jang, C.-W. Kim, Exosomes derived from mesenchymal stem cells suppress angiogenesis by down-regulating VEGF expression in breast cancer cells, PLoS One 8 (12) (2013) e84256.
[13] J. Rak, A. Guha, Extracellular vesicles—vehicles that spread cancer genes, Bioessays 34 (6) (2012) 489–497.
[14] E. D'Asti, D. Garnier, T.H. Lee, L. Montermini, B. Meehan, J. Rak, Oncogenic extracellular vesicles in brain tumor progression, Front. Physiol. 3 (2012) 294.
[15] I.-H. Chen, L. Xue, C.-C. Hsu, J.S.P. Paez, L. Pan, H. Andaluz, M.K. Wendt, A.B. Iliuk, J.-K. Zhu, W.A. Tao, Phosphoproteins in extracellular vesicles as candidate markers for breast cancer, Proc. Natl. Acad. Sci. Unit. States Am. (2017) 201618088.
[16] V. Kralj-Iglic, Stability of membranous nanostructures: a possible key mechanism in cancer progression, Int. J. Nanomed. 7 (2012) 3579.
[17] J. Ratajczak, M. Wysoczynski, F. Hayek, A. Janowska-Wieczorek, M. Ratajczak, Membrane-derived microvesicles: important and underappreciated mediators of cell-to-cell communication, Leukemia 20 (9) (2006) 1487.
[18] K. Gousset, E. Schiff, C. Langevin, Z. Marijanovic, A. Caputo, D.T. Browman, N. Chenouard, F. De Chaumont, A. Martino, J. Enninga, Prions hijack tunnelling nanotubes for intercellular spread, Nat. Cell Biol. 11 (3) (2009) 328.
[19] C.F. Reich III, D.S. Pisetsky, The content of DNA and RNA in microparticles released by Jurkat and HL-60 cells undergoing in vitro apoptosis, Exp. Cell Res. 315 (5) (2009) 760–768.
[20] M. Nawaz, F. Fatima, Extracellular vesicles, tunneling nanotubes, and cellular interplay: synergies and missing links, Front. Mol. Biosci. 4 (2017) 50.
[21] N. Coltel, V. Combes, S.C. Wassmer, G. Chimini, G.E. Grau, Cell vesiculation and immunopathology: implications in cerebral malaria, Microb. Infect. 8 (8) (2006) 2305–2316.
[22] V. Kralj-Iglič, A. Iglič, H. Hägerstrand, M. Bobrowska-Hägerstrand, Hypothesis of nanostructures of cell and phospholipid membranes as cell infrastructure, Med. Razgl. 44 (2005) 155–169.
[23] V. Šuštar, A. Bedina-Zavec, R. Štukelj, M. Frank, G. Bobojević, R. Janša, E. Ogorevc, P. Kruljc, K. Mam, B. Šimunič, Nanoparticles isolated from blood: a reflection of vesiculability of blood cells during the isolation process, Int. J. Nanomed. 6 (2011) 2737.
[24] V. Suštar, A. Bedina-Zavec, R. Stukelj, M. Frank, E. Ogorevc, R. Janša, K. Mam, P. Veranič, V. Kralj-Iglič, Post-prandial rise of microvesicles in peripheral blood of healthy human donors, Lipids Health Dis. 10 (2011) 47.
[25] C.W. Kim, H.M. Lee, T.H. Lee, C. Kang, H.K. Kleinman, Y.S. Gho, Extracellular membrane vesicles from tumor cells promote angiogenesis via sphingomyelin, Cancer Res. 62 (21) (2002) 6312–6317.
[26] H. Valadi, K. Ekström, A. Bossios, M. Sjöstrand, J.J. Lee, J.O. Lötvall, Exosome-mediated transfer of mRNAs and microRNAs is a novel mechanism of genetic exchange between cells, Nat. Cell Biol. 9 (6) (2007) 654.
[27] E.R. Sauter, N. Patel, Body fluid micro (mi) RNAs as biomarkers for human cancer, J. Nucleic Acids Invest. 2 (1) (2011) 1.
[28] J. Lu, G. Getz, E.A. Miska, E. Alvarez-Saavedra, J. Lamb, D. Peck, A. Sweet-Cordero, B.L. Ebert, R.H. Mak, A.A. Ferrando, MicroRNA expression profiles classify human cancers, Nature 435 (7043) (2005) 834.
[29] B.S. Nielsen, S. Jørgensen, J.U. Fog, R. Søkilde, I.J. Christensen, U. Hansen, N. Brünner, A. Baker, S. Møller, H.J. Nielsen, High levels of microRNA-21 in

the stroma of colorectal cancers predict short disease-free survival in stage II colon cancer patients, Clin. Exp. Metastasis 28 (1) (2011) 27–38.
[30] L.E. Graves, E.V. Ariztia, J.R. Navari, H.J. Matzel, M.S. Stack, D.A. Fishman, Proinvasive properties of ovarian cancer ascites-derived membrane vesicles, Cancer Res. 64 (19) (2004) 7045–7049.
[31] C. Gercel-Taylor, S. Atay, R.H. Tullis, M. Kesimer, D.D. Taylor, Nanoparticle analysis of circulating cell-derived vesicles in ovarian cancer patients, Anal. Biochem. 428 (1) (2012) 44–53.
[32] M.T. Le, P. Hamar, C. Guo, E. Basar, R. Perdigão-Henriques, L. Balaj, J. Lieberman, miR-200–containing extracellular vesicles promote breast cancer cell metastasis, J. Clin. Invest. 124 (12) (2014) 5109–5128.
[33] X. Ma, Z. Chen, D. Hua, D. He, L. Wang, P. Zhang, J. Wang, Y. Cai, C. Gao, X. Zhang, Essential role for TrpC5-containing extracellular vesicles in breast cancer with chemotherapeutic resistance, Proc. Natl. Acad. Sci. Unit. States Am. 111 (17) (2014) 6389–6394.
[34] E. Lázaro-Ibáñez, A. Sanz-Garcia, T. Visakorpi, C. Escobedo-Lucea, P. Siljander, Á. Ayuso-Sacido, M. Yliperttula, Different gDNA content in the subpopulations of prostate cancer extracellular vesicles: apoptotic bodies, microvesicles, and exosomes, Prostate 74 (14) (2014) 1379–1390.
[35] D.-S. Choi, D.-Y. Choi, B. Hong, S. Jang, D.-K. Kim, J. Lee, Y.-K. Kim, K. Pyo Kim, Y. Gho, Quantitative proteomics of extracellular vesicles derived from human primary and metastatic colorectal cancer cells, J. Extracell. Vesicles 1 (1) (2012) 18704.
[36] K. Takahashi, I.K. Yan, T. Kogure, H. Haga, T. Patel, Extracellular vesicle-mediated transfer of long non-coding RNA ROR modulates chemosensitivity in human hepatocellular cancer, FEBS Open Bio. 4 (1) (2014) 458–467.
[37] D.K. Jeppesen, A. Nawrocki, S.G. Jensen, K. Thorsen, B. Whitehead, K.A. Howard, L. Dyrskjøt, T.F. Ørntoft, M.R. Larsen, M.S. Ostenfeld, Quantitative proteomics of fractionated membrane and lumen exosome proteins from isogenic metastatic and nonmetastatic bladder cancer cells reveal differential expression of EMT factors, Proteomics 14 (6) (2014) 699–712.
[38] S.A. Melo, L.B. Luecke, C. Kahlert, A.F. Fernandez, S.T. Gammon, J. Kaye, V.S. LeBleu, E.A. Mittendorf, J. Weitz, N. Rahbari, Glypican-1 identifies cancer exosomes and detects early pancreatic cancer, Nature 523 (7559) (2015) 177.
[39] A. Janowska-Wieczorek, M. Wysoczynski, J. Kijowski, L. Marquez-Curtis, B. Machalinski, J. Ratajczak, M.Z. Ratajczak, Microvesicles derived from activated platelets induce metastasis and angiogenesis in lung cancer, Int. J. Canc. 113 (5) (2005) 752–760.
[40] A. Mrvar-Brečko, V. Šuštar, V. Janša, R. Štukelj, R. Janša, E. Mujagić, P. Kruljc, A. Iglič, H. Hägerstrand, V. Kralj-Iglič, Isolated microvesicles from peripheral blood and body fluids as observed by scanning electron microscope, Blood Cells Mol. Dis. 44 (4) (2010) 307–312.
[41] S.A. Kooijmans, P. Vader, S.M. van Dommelen, W.W. van Solinge, R.M. Schiffelers, Exosome mimetics: a novel class of drug delivery systems, Int. J. Nanomed. 7 (2012) 1525.
[42] S.J. Singer, G.L. Nicolson, The fluid mosaic model of the structure of cell membranes, Science 175 (4023) (1972) 720–731.
[43] L.J. Pike, Rafts defined: a report on the keystone symposium on lipid rafts and cell function, J. Lipid Res. 47 (7) (2006) 1597–1598.
[44] M. Chabanon, P. Rangamani, Gaussian curvature directs the distribution of spontaneous curvature on bilayer membrane necks, Soft Matter 14 (12) (2018) 2281–2294.
[45] D. Jesenek, A. Iglic, V. kralj-iglic, S. Kralj, Orientational order within biological membranes, Int. Rev. Biochem. 3 (2012) 157–162.

[46] H. Hägerstrand, L. Mrówczyńska, U. Salzer, R. Prohaska, K.A. Michelsen, V. Kralj-Iglič, A. Iglič, Curvature-dependent lateral distribution of raft markers in the human erythrocyte membrane, Mol. Membr. Biol. 23 (3) (2006) 277–288.
[47] B. Deuticke, Transformation and restoration of biconcave shape of human erythrocytes induced by amphiphilic agents and changes of ionic environment, Biochim. Biophys. Acta Biomembr. 163 (4) (1968) 494–500.
[48] M.P. Sheetz, S.J. Singer, Biological membranes as bilayer couples. A molecular mechanism of drug-erythrocyte interactions, Proc. Natl. Acad. Sci. Unit. States Am. 71 (11) (1974) 4457–4461.
[49] F. MacKintosh, T. Lubensky, Orientational order, topology, and vesicle shapes, Phys. Rev. Lett. 67 (9) (1991) 1169.
[50] V. Kralj-Iglič, A. Iglič, H. Hägerstrand, P. Peterlin, Stable tubular microexovesicles of the erythrocyte membrane induced by dimeric amphiphiles, Phys. Rev. 61 (4) (2000) 4230.
[51] V. Kralj-Iglič, B. Babnik, D.R. Gauger, S. May, A. Iglič, Quadrupolar ordering of phospholipid molecules in narrow necks of phospholipid vesicles, J. Stat. Phys. 125 (3) (2006) 727–752.
[52] A. Iglič, D. Drobne, V. Kralj-Iglič, Nanostructures in Biological Systems: Theory and Applications, Pan Stanford, 2015.
[53] D. Kabaso, N. Bobrovska, W. Góźdź, N. Gov, V. Kralj-Iglič, P. Veranič, A. Iglič, On the role of membrane anisotropy and BAR proteins in the stability of tubular membrane structures, J. Biomech. 45 (2) (2012) 231–238.
[54] V. Kralj-Iglič, V. Heinrich, S. Svetina, B. Žekš, Free energy of closed membrane with anisotropic inclusions, Euro. Phys. J. B 10 (1) (1999) 5–8.
[55] V. Kralj-Iglič, S. Svetina, B. Žekž, Shapes of bilayer vesicles with membrane embedded molecules, Eur. Biophys. J. 24 (5) (1996) 311–321.
[56] J. Fournier, Nontopological saddle-splay and curvature instabilities from anisotropic membrane inclusions, Phys. Rev. Lett. 76 (23) (1996) 4436.
[57] T. Baumgart, B.R. Capraro, C. Zhu, S.L. Das, Thermodynamics and mechanics of membrane curvature generation and sensing by proteins and lipids, Annu. Rev. Phys. Chem. 62 (2011) 483–506.
[58] A. Tian, T. Baumgart, Sorting of lipids and proteins in membrane curvature gradients, Biophys. J. 96 (7) (2009) 2676–2688.
[59] J. Zimmerberg, M.M. Kozlov, How proteins produce cellular membrane curvature, Nat. Rev. Mol. Cell Biol. 7 (1) (2006) 9.
[60] J. Gómez-Llobregat, F. Elías-Wolff, M. Lindén, Anisotropic membrane curvature sensing by amphipathic peptides, Biophys. J. 110 (1) (2016) 197–204.
[61] L. Mesarec, W. Góźdź, V.K. Iglič, S. Kralj, A. Iglič, Closed membrane shapes with attached BAR domains subject to external force of actin filaments, Colloids Surfaces B Biointerfaces 141 (2016) 132–140.
[62] M. Simunovic, G.A. Voth, A. Callan-Jones, P. Bassereau, When physics takes over: BAR proteins and membrane curvature, Trends Cell Biol. 25 (12) (2015) 780–792.
[63] A. Frost, V.M. Unger, P. De Camilli, The BAR domain superfamily: membrane-molding macromolecules, Cell 137 (2) (2009) 191–196.
[64] J.F. Nagle, S. Tristram-Nagle, Structure of lipid bilayers, Biochim. Biophys. Acta Rev. Biomembr. 1469 (3) (2000) 159–195.
[65] K. Bacia, P. Schwille, T. Kurzchalia, Sterol structure determines the separation of phases and the curvature of the liquid-ordered phase in model membranes, Proc. Natl. Acad. Sci. Unit. States Am. 102 (9) (2005) 3272–3277.
[66] R. Oda, I. Huc, M. Schmutz, S. Candau, F. MacKintosh, Tuning bilayer twist using chiral counterions, Nature 399 (6736) (1999) 566.

[67] W. Helfrich, J. Prost, Intrinsic bending force in anisotropic membranes made of chiral molecules, Phys. Rev. 38 (6) (1988) 3065.
[68] S. Koehler, V. Schaller, A.R. Bausch, Collective dynamics of active cytoskeletal networks, PLoS One 6 (8) (2011) e23798.
[69] W. Helfrich, Elastic properties of lipid bilayers: theory and possible experiments, Z. Naturforsch. C Biosci. 28 (11–12) (1973) 693–703.
[70] M.C. Watson, E.S. Penev, P.M. Welch, F.L. Brown, Thermal fluctuations in shape, thickness, and molecular orientation in lipid bilayers, J. Chem. Phys. 135 (24) (2011) 244701.
[71] T. Lubensky, J. Prost, Orientational order and vesicle shape, J. Phys. II 2 (3) (1992) 371–382.
[72] G. Smith, E. Sirota, C. Safinya, N.A. Clark, Structure of the L β phases in a hydrated phosphatidylcholine multimembrane, Phys. Rev. Lett. 60 (9) (1988) 813.
[73] U. Bernchou, J. Brewer, H.S. Midtiby, J.H. Ipsen, L.A. Bagatolli, A.C. Simonsen, Texture of lipid bilayer domains, J. Am. Chem. Soc. 131 (40) (2009) 14130–14131.
[74] L. Mesarec, W. Góźdź, S. Kralj, M. Fošnarič, S. Penič, V. Kralj-Iglič, A. Iglič, On the role of external force of actin filaments in the formation of tubular protrusions of closed membrane shapes with anisotropic membrane components, Eur. Biophys. J. 46 (8) (2017) 705–718.
[75] S. Kralj, R. Rosso, E.G. Virga, Curvature control of valence on nematic shells, Soft Matter 7 (2) (2011) 670–683.
[76] R.D. Kamien, The geometry of soft materials: a primer, Rev. Mod. Phys. 74 (4) (2002) 953.
[77] M.V.e. Kurik, O. Lavrentovich, Defects in liquid crystals: homotopy theory and experimental studies, Phys. Usp. 31 (3) (1988) 196–224.
[78] N.D. Mermin, The topological theory of defects in ordered media, Rev. Mod. Phys. 51 (3) (1979) 591.
[79] D. Jesenek, Š. Perutková, V. Kralj-Iglič, S. Kralj, A. Iglič, Exocytotic fusion pore stability and topological defects in the membrane with orientational degree of ordering, Cell Calcium 52 (3–4) (2012) 277–282.
[80] W.T. Snead, C.C. Hayden, A.K. Gadok, C. Zhao, E.M. Lafer, P. Rangamani, J.C. Stachowiak, Membrane fission by protein crowding, Proc. Natl. Acad. Sci. Unit. States Am. 114 (16) (2017) E3258–E3267.
[81] N. Ramakrishnan, P.S. Kumar, J.H. Ipsen, Membrane-mediated aggregation of curvature-inducing nematogens and membrane tubulation, Biophys. J. 104 (5) (2013) 1018–1028.
[82] N. Ramakrishnan, P.S. Kumar, J.H. Ipsen, Monte Carlo simulations of fluid vesicles with in-plane orientational ordering, Phys. Rev. 81 (4) (2010) 041922.
[83] N. Ramakrishnan, J.H. Ipsen, P.S. Kumar, Role of disclinations in determining the morphology of deformable fluid interfaces, Soft Matter 8 (11) (2012) 3058–3061.
[84] D.R. Nelson, Toward a tetravalent chemistry of colloids, Nano Lett. 2 (10) (2002) 1125–1129.
[85] D. Seč, T. Lopez-Leon, M. Nobili, C. Blanc, A. Fernandez-Nieves, M. Ravnik, S. Žumer, Defect trajectories in nematic shells: role of elastic anisotropy and thickness heterogeneity, Phys. Rev. 86 (2) (2012) 020705.
[86] G. Skačej, C. Zannoni, Controlling surface defect valence in colloids, Phys. Rev. Lett. 100 (19) (2008) 197802.
[87] V. Vitelli, D.R. Nelson, Nematic textures in spherical shells, Phys. Rev. 74 (2) (2006) 021711.
[88] L. Mesarec, P. Kurioz, A. Iglič, W. Góźdź, S. Kralj, Curvature-controlled topological defects, Crystals 7 (6) (2017) 153.

[89] R. Rosso, E. Virga, S. Kralj, Parallel transport and defects on nematic shells, Continum. Mech. Thermodyn. 24 (2012) 643.
[90] L. Mesarec, W. Góźdź, A. Iglič, S. Kralj, Effective topological charge cancelation mechanism, Sci. Rep. 6 (2016) 27117.
[91] E.A. Evans, Bending resistance and chemically induced moments in membrane bilayers, Biophys. J. 14 (12) (1974) 923–931.
[92] H. Deuling, W. Helfrich, Red blood cell shapes as explained on the basis of curvature elasticity, Biophys. J. 16 (8) (1976) 861–868.
[93] A. Boulbitch, R. Simson, D. Simson, R. Merkel, W. Häckl, M. Bärmann, E. Sackmann, Shape instability of a biomembrane driven by a local softening of the underlying actin cortex, Phys. Rev. 62 (3) (2000) 3974.
[94] L. Mesarec, M. Fošnarič, S. Penič, V. Kralj Iglič, S. Kralj, W. Góźdź, A. Iglič, Numerical study of membrane configurations, Adv. Condens. Matter Phys. 2014 (2014).
[95] Z. Shi, T. Baumgart, Dynamics and instabilities of lipid bilayer membrane shapes, Adv. Colloid Interface Sci. 208 (2014) 76–88.
[96] D. Bochicchio, L. Monticelli, The membrane bending modulus in experiments and simulations: a puzzling picture, in: Advances in Biomembranes and Lipid Self-Assembly, Elsevier, 2016, pp. 117–143.
[97] Z.A. Levine, R.M. Venable, M.C. Watson, M.G. Lerner, J.-E. Shea, R.W. Pastor, F.L. Brown, Determination of biomembrane bending moduli in fully atomistic simulations, J. Am. Chem. Soc. 136 (39) (2014) 13582–13585.
[98] M.C. Watson, E.G. Brandt, P.M. Welch, F.L. Brown, Determining biomembrane bending rigidities from simulations of modest size, Phys. Rev. Lett. 109 (2) (2012) 028102.
[99] V. Kralj-Iglic, A. Iglic, G. Gomiscek, F. Sevsek, V. Arrigler, H. Hägerstrand, Microtubes and nanotubes of a phospholipid bilayer membrane, J. Phys. Math. Gen. 35 (7) (2002) 1533.
[100] A. Iglič, B. Babnik, U. Gimsa, V. Kralj-Iglič, On the role of membrane anisotropy in the beading transition of undulated tubular membrane structures, J. Phys. Math. Gen. 38 (40) (2005) 8527.
[101] V. Kralj-Iglič, M. Remškar, G. Vidmar, M. Fošnarič, A. Iglič, Deviatoric elasticity as a possible physical mechanism explaining collapse of inorganic micro and nanotubes, Phys. Lett. 296 (2–3) (2002) 151–155.
[102] G. Napoli, L. Vergori, Surface free energies for nematic shells, Phys. Rev. 85 (6) (2012) 061701.
[103] G. Napoli, L. Vergori, Extrinsic curvature effects on nematic shells, Phys. Rev. Lett. 108 (20) (2012) 207803.
[104] T.-S. Nguyen, J. Geng, R.L. Selinger, J.V. Selinger, Nematic order on a deformable vesicle: theory and simulation, Soft Matter 9 (34) (2013) 8314–8326.
[105] R.L.B. Selinger, A. Konya, A. Travesset, J.V. Selinger, Monte Carlo studies of the XY model on two-dimensional curved surfaces, J. Phys. Chem. B 115 (48) (2011) 13989–13993.
[106] W. Góźdź, Spontaneous curvature induced shape transformations of tubular polymersomes, Langmuir 20 (18) (2004) 7385–7391.
[107] W. Góźdź, Influence of spontaneous curvature and microtubules on the conformations of lipid vesicles, J. Phys. Chem. B 109 (44) (2005) 21145–21149.
[108] O.D. Lavrentovich, Topological defects in dispersed words and worlds around liquid crystals, or liquid crystal drops, Liq. Cryst. 24 (1) (1998) 117–126.
[109] C.-M. Chen, P. Higgs, F. MacKintosh, Theory of fission for two-component lipid vesicles, Phys. Rev. Lett. 79 (8) (1997) 1579.

[110] L. Miao, U. Seifert, M. Wortis, H.-G. Döbereiner, Budding transitions of fluid-bilayer vesicles: the effect of area-difference elasticity, Phys. Rev. 49 (6) (1994) 5389.
[111] U. Seifert, Configurations of fluid membranes and vesicles, Adv. Phys. 46 (1) (1997) 13–137.
[112] A. Iglič, B. Babnik, K. Bohinc, M. Fošnarič, H. Hägerstrand, V. Kralj-Iglič, On the role of anisotropy of membrane constituents in formation of a membrane neck during budding of a multicomponent membrane, J. Biomech. 40 (3) (2007) 579–585.
[113] O.C. Farokhzad, R. Langer, Nanomedicine: developing smarter therapeutic and diagnostic modalities, Adv. Drug Deliv. Rev. 58 (14) (2006) 1456–1459.
[114] I. Brigger, C. Dubernet, P. Couvreur, Nanoparticles in cancer therapy and diagnosis, Adv. Drug Deliv. Rev. 64 (2012) 24–36.
[115] M.K. Yu, J. Park, S. Jon, Targeting strategies for multifunctional nanoparticles in cancer imaging and therapy, Theranostics 2 (1) (2012) 3.
[116] J. Xie, S. Lee, X. Chen, Nanoparticle-based theranostic agents, Adv. Drug Deliv. Rev. 62 (11) (2010) 1064–1079.
[117] A.J. Cole, V.C. Yang, A.E. David, Cancer theranostics: the rise of targeted magnetic nanoparticles, Trends Biotechnol. 29 (7) (2011) 323–332.
[118] E.J.G.J. Dolmans, D. Fukumura, R.K. Jain, Photodynamic therapy for cancer, Nat. Rev. Canc. 3 (2003) 380–387.
[119] S. Wang, R. Gao, F. Zhou, M. Selke, Nanomaterials and singlet oxygen photosensitizers: potential applications in photodynamic therapy, J. Mater. Chem. 14 (4) (2004) 487–493.
[120] M.B. Askari, Z. Tavakoli, M. Seifi, s. Bagheri, P. Veisi, Synthesis of TiO_2 nanoparticles and decorated multi-wall carbon nanotube (MWCNT) with anatase TiO_2 nanoparticles and study of optical properties and structural characterization of TiO_2/MWCNT nanocomposite, Optik 149 (2017).
[121] Z. Fei Yin, L. Wu, H. Gui Yang, Y. Hua Su, Recent progress in biomedical applications of titanium dioxide, Phys. Chem. Chem. Phys. 15 (14) (2013) 4844–4858.
[122] T. Rajh, N.M. Dimitrijevic, M. Bissonnette, T. Koritarov, V. Konda, Titanium dioxide in the service of the biomedical revolution, Chem. Rev. 114 (19) (2014) 10177–10216.
[123] R. Imani, M. Pazoki, D. Zupančič, M.E. Kreft, V. Kralj-Iglič, P. Veranič, A. Iglič, Biocompatibility of different nanostructured TiO_2 scaffolds and their potential for urologic applications, Protoplasma 253 (6) (2016) 1439–1447.
[124] T. Tachikawa, T. Majima, Single-molecule, single-particle fluorescence imaging of TiO_2-based photocatalytic reactions, Chem. Soc. Rev. 39 (12) (2010) 4802–4819.
[125] J. Schneider, M. Matsuoka, M. Takeuchi, J. Zhang, Y. Horiuchi, M. Anpo, D.W. Bahnemann, Understanding TiO_2 photocatalysis: mechanisms and materials, Chem. Rev. 114 (19) (2014) 9919–9986.
[126] R. Imani, V. Kralj-Iglič, A. Iglič, Chapter seven - TiO_2 nanostructures in biomedicine, in: A. Iglič, C.V. Kulkarni, M. Rappolt (Eds.), Advances in Biomembranes and Lipid Self-Assembly, Academic Press, 2016, pp. 163–207.
[127] R. Imani, Synthesis of TiO_2 Nanomaterials as Multifunctional Materials for Biomedical Application: An Experimental Investigation, Doctoral Thesis, Ljubljana, 2015.
[128] Y. Kubota, T. Shuin, C. Kawasaki, M. Hosaka, H. Kitamura, R. Cai, H. Sakai, K. Hashimoto, A. Fujishima, Photokilling of T-24 human bladder cancer cells with titanium dioxide, Br. J. Canc. 70 (6) (1994) 1107–1111.
[129] R. Cai, Y. Kubota, T. Shuin, H. Sakai, K. Hashimoto, A. Fujishima, Induction of cytotoxicity by photoexcited TiO_2 particles, Cancer Res. 52 (8) (1992) 2346–2348.

[130] Z. Hu, Y. Huang, S. Sun, W. Guan, Y. Yao, P. Tang, C. Li, Visible light driven photodynamic anticancer activity of graphene oxide/TiO_2 hybrid, Carbon 50 (3) (2012) 994–1004.
[131] R. Imani, P. Veranič, A. Iglič, M.E. Kreft, M. Pazoki, S. Hudoklin, Combined cytotoxic effect of UV-irradiation and TiO_2 microbeads in normal urothelial cells, low-grade and high-grade urothelial cancer cells, Photochem. Photobiol. Sci. 14 (3) (2015) 583–590.
[132] M. Song, R. Zhang, Y. Dai, F. Gao, H. Chi, G. Lv, B. Chen, X. Wang, The in vitro inhibition of multidrug resistance by combined nanoparticulate titanium dioxide and UV irradiation, Biomaterials 27 (23) (2006) 4230–4238.
[133] M. Xu, N. Huang, Z. Xiao, Z. Lu, Photoexcited TiO_2 nanoparticles through •OH-radicals induced malignant cells to necrosis, Supramol. Sci. 5 (5–6) (1998) 449–451.
[134] J. Xu, Y. Sun, Y. Zhao, J. Huang, C. Chen, Z. Jiang, Photocatalytic inactivation effect of gold-doped TiO_2 (Au/TiO_2) nanocomposites on human colon carcinoma LoVo cells, Int. J. Photoenergy 2007 (2007).
[135] N. Lagopati, P. Kitsiou, A. Kontos, P. Venieratos, E. Kotsopoulou, A. Kontos, D. Dionysiou, S. Pispas, E. Tsilibary, P. Falaras, Photo-induced treatment of breast epithelial cancer cells using nanostructured titanium dioxide solution, J. Photochem. Photobiol. Chem. 214 (2–3) (2010) 215–223.
[136] C. Wang, S. Cao, X. Tie, B. Qiu, A. Wu, Z. Zheng, Induction of cytotoxicity by photoexcitation of TiO_2 can prolong survival in glioma-bearing mice, Mol. Biol. Rep. 38 (1) (2011) 523–530.
[137] J. Petković, T. Küzma, K. Rade, S. Novak, M. Filipič, Pre-irradiation of anatase TiO_2 particles with UV enhances their cytotoxic and genotoxic potential in human hepatoma HepG2 cells, J. Hazard Mater. 196 (2011) 145–152.
[138] J. Rauch, W. Kolch, S. Laurent, M. Mahmoudi, Big signals from small particles: regulation of cell signaling pathways by nanoparticles, Chem. Rev. 113 (5) (2013) 3391–3406.
[139] H. Sakai, R. Baba, K. Hashimoto, Y. Kubota, A. Fujishima, Selective killing of a single cancerous T24 cell with TiO_2 semiconducting microelectrode under irradiation, Chem. Lett. 24 (3) (1995) 185–186.
[140] D. Trachootham, J. Alexandre, P. Huang, Targeting cancer cells by ROS-mediated mechanisms: a radical therapeutic approach? Nat. Rev. Drug Discov. 8 (7) (2009) 579.
[141] N. Wu, J. Wang, D.N. Tafen, H. Wang, J.-G. Zheng, J.P. Lewis, X. Liu, S.S. Leonard, A. Manivannan, Shape-enhanced photocatalytic activity of single-crystalline anatase TiO_2 (101) nanobelts, J. Am. Chem. Soc. 132 (19) (2010) 6679–6685.
[142] J.w. Seo, H. Chung, M.y. Kim, J. Lee, I.h. Choi, J. Cheon, Development of water-soluble single-crystalline TiO_2 nanoparticles for photocatalytic cancer-cell treatment, Small 3 (5) (2007) 850–853.
[143] M. Pazoki, N. Taghavinia, A. Hagfeldt, G. Boschloo, Mesoporous TiO_2 microbead electrodes for cobalt-mediator-based dye-sensitized solar cells, J. Phys. Chem. C 118 (30) (2014) 16472–16478.
[144] R. Imani, A. Iglič, A.P. Turner, A. Tiwari, Electrochemical detection of DNA damage through visible-light-induced ROS using mesoporous TiO_2 microbeads, Electrochem. Commun. 40 (2014) 84–87.
[145] V. Kononenko, R. Imani, N. Repar, M. Benčina, M. Lorenzetti, A. Erman, D. Drobne, A. Iglič, Chapter four - phototoxicity of mesoporous TiO_2+Gd microbeads with theranostic potential, in: A. Iglič, M. Rappolt, A.J. García-Sáez (Eds.), Advances in Biomembranes and Lipid Self-Assembly, Academic Press, 2017, pp. 153–171.

[146] R. Imani, M. Pazoki, A. Tiwari, G. Boschloo, A.P. Turner, V. Kralj-Iglič, A. Iglič, Band edge engineering of TiO_2@ DNA nanohybrids and implications for capacitive energy storage devices, Nanoscale 7 (23) (2015) 10438−10448.
[147] H.K. Patra, R. Imani, J.R. Jangamreddy, M. Pazoki, A. Iglič, A.P. Turner, A. Tiwari, On/off-switchable anti-neoplastic nanoarchitecture, Sci. Rep. 5 (2015) 14571.
[148] R. Imani, V. Kralj-Iglič, A. Iglič, TiO_2 nanostructures in biomedicine, in: Advances in Biomembranes and Lipid Self-Assembly, Elsevier, 2016, pp. 163−207.
[149] A.D. Maynard, Don't define nanomaterials, Nature 475 (7354) (2011) 31.
[150] M.E. Kreft, M. Sterle, P. Veranič, K. Jezernik, Urothelial injuries and the early wound healing response: tight junctions and urothelial cytodifferentiation, Histochem. Cell Biol. 123 (4−5) (2005) 529−539.
[151] C. Hafner, R. Knuechel, R. Stoehr, A. Hartmann, Clonality of multifocal urothelial carcinomas: 10 years of molecular genetic studies, Int. J. Canc. 101 (1) (2002) 1−6.
[152] M.G. Wientjes, R.A. Badalament, R.C. Wang, F. Hassan, J.L. Au, Penetration of mitomycin C in human bladder, Cancer Res. 53 (14) (1993) 3314−3320.
[153] M.E. Kreft, K. Jezernik, M. Kreft, R. Romih, Apical plasma membrane traffic in superficial cells of bladder urothelium, Ann. N. Y. Acad. Sci. 1152 (1) (2009) 18−29.
[154] M. Li, H. Deng, H.-S. Peng, Q. Wang, Functional nanoparticles in targeting glioma diagnosis and therapies, J. Nanosci. Nanotechnol. 14 (2014) 415−432.
[155] F. Jia, X. Liu, L. Li, S. Mallapragada, B. Narasimhan, Q. Wang, Multifunctional nanoparticles for targeted delivery of immune activating and cancer therapeutic agents, J. Contr. Release 172 (3) (2013) 1020−1034.
[156] H. Dong, G. Zeng, L. Tang, C. Fan, C. Zhang, X. He, Y. He, An overview on limitations of TiO_2-based particles for photocatalytic degradation of organic pollutants and the corresponding countermeasures, Water Res. 79 (2015) 128−146.
[157] F. Wang, W.B. Tan, Y. Zhang, X. Fan, M. Wang, Luminescent nanomaterials for biological labelling, Nanotechnology 17 (1) (2005) R1.
[158] H.B. Na, I.C. Song, T. Hyeon, Inorganic nanoparticles for MRI contrast agents, Adv. Mater. 21 (21) (2009) 2133−2148.
[159] M.S. Eljamel, Fluorescence image-guided surgery of brain tumors: explained step-by-step, Photodiagn. Photodyn. Ther. 5 (4) (2008) 260−263.
[160] M. Longmire, P.L. Choyke, H. Kobayashi, Clearance Properties of Nano-Sized Particles and Molecules as Imaging Agents: Considerations and Caveats, 2008.
[161] M.C. Heffern, L.M. Matosziuk, T.J. Meade, Lanthanide probes for bioresponsive imaging, Chem. Rev. 114 (8) (2013) 4496−4539.
[162] J. Lohrke, T. Frenzel, J. Endrikat, F.C. Alves, T.M. Grist, M. Law, J.M. Lee, T. Leiner, K.-C. Li, K. Nikolaou, 25 years of contrast-enhanced MRI: developments, current challenges and future perspectives, Adv. Ther. 33 (1) (2016) 1−28.
[163] X. Chen, W. Luo, Optical spectroscopy of rare earth ion-doped TiO_2 nanophosphors, J. Nanosci. Nanotechnol. 10 (3) (2010) 1482−1494.
[164] J.Z. Bloh, R. Dillert, D.W. Bahnemann, Designing optimal metal-doped photocatalysts: correlation between photocatalytic activity, doping ratio, and particle size, J. Phys. Chem. C 116 (48) (2012) 25558−25562.
[165] L. Li, C.K. Tsung, Z. Yang, G.D. Stucky, L. Sun, J. Wang, C. Yan, Rare-earth-doped nanocrystalline titania microspheres emitting luminescence via energy transfer, Adv. Mater. 20 (5) (2008) 903−908.
[166] Y. Mosesson, G.B. Mills, Y. Yarden, Derailed endocytosis: an emerging feature of cancer, Nat. Rev. Canc. 8 (11) (2008) 835.
[167] R.A. Petros, J.M. DeSimone, Strategies in the design of nanoparticles for therapeutic applications, Nat. Rev. Drug Discov. 9 (8) (2010) 615.
[168] W. Góźdź, Deformations of lipid vesicles induced by attached spherical particles, Langmuir 23 (10) (2007) 5665−5669.

[169] S.A. Nowak, T. Chou, Membrane lipid segregation in endocytosis, Phys. Rev. 78 (2) (2008) 021908.
[170] M. Fošnarič, A. Iglič, D.M. Kroll, S. May, Monte Carlo simulations of complex formation between a mixed fluid vesicle and a charged colloid, J. Chem. Phys. 131 (10) (2009) 09B610.
[171] D. Jesenek, Š. Perutková, W. Góźdź, V. Kralj-Iglič, A. Iglič, S. Kralj, Vesiculation of biological membrane driven by curvature induced frustrations in membrane orientational ordering, Int. J. Nanomed. 8 (1) (2013) 677−687.
[172] H.m. Ding, Y.q. Ma, Theoretical and computational investigations of nanoparticle−biomembrane interactions in cellular delivery, Small 11 (9−10) (2015) 1055−1071.
[173] M. Deserno, Elastic deformation of a fluid membrane upon colloid binding, Phys. Rev. 69 (3) (2004) 031903.
[174] M. Deserno, T. Bickel, Wrapping of a spherical colloid by a fluid membrane, Europhys. Lett. 62 (5) (2003) 767.
[175] D. Harries, A. Ben-Shaul, I. Szleifer, Enveloping of charged proteins by lipid bilayers, J. Phys. Chem. B 108 (4) (2004) 1491−1496.
[176] M. Deserno, When do fluid membranes engulf sticky colloids? J. Phys. Condens. Matter 16 (22) (2004) S2061.